doi: 10.32131/jes.1.8

Journal of the Earth Simulator, Volume 1, April 2004, 8–34

10-km Mesh Meso-scale Resolving Simulations of the Global Atmosphere on the Earth Simulator

– Preliminary Outcomes of AFES (AGCM for the Earth Simulator) –

Wataru Ohfuchi[1]*, Hisashi Nakamura[2, 3], Mayumi K. Yoshioka[1], Takeshi Enomoto[1],
Koutarou Takaya[2], Xindong Peng[1], Shozo Yamane[2], Teruyuki Nishimura[2], Yoshio Kurihara[2]
and Kozo Ninomiya[2]

[1] *The Earth Simulator Center, Japan Agency for Marine-Earth Science and Technology, Yokohama, Japan*
[2] *Frontier Research System for Global Change, Japan Agency for Marine-Earth Science and Technology, Yokohama, Japan*
[3] *Department of Earth and Planetary Science, the University of Tokyo, Tokyo, Japan*

(Received February 9, 2004; Revised manuscript accepted April 26, 2004)

Abstract In early March of 2002, a massively-parallel-vector supercomputer, the Earth Simulator, came into operation, providing a unique opportunity to perform simulations of the general circulation of the global atmosphere with horizontal resolution of about 10 km. We employ a general circulation model called “AFES” that has been fully optimized to the unique architecture of the Earth Simulator, to attain extremely high computational efficiency. The ultra-high resolution global simulations with AFES are able to explicitly represent interaction among planetary, synoptic and meso-scale phenomena and the topographic modulation of mesoscale precipitation without the need to nest a regional mesoscale model. Examples are presented of wintertime extratropical cyclogenesis in the North Pacific, a polar low over the Sea of Japan, pre-summer Baiu frontal zone over Japan and typhoon evolution over the western North Pacific, to show that mesoscale precipitation systems and their interactions with synoptic and planetary scale flows and topography are indeed simulated in a fairly realistic manner. Filamentary evolution of potential vorticity within an upper-level trough and its coupling with the underlying frontal evolution or polar-low development are also simulated.

Keywords: Global meso-scale resolving atmospheric model, ultra high resolution global atmospheric simulation, high-performace computing in meteorology, the Earth Simulator

1. Introduction

Comprehensive numerical simulation of the atmosphere for both weather forecasting, and studies of the general circulation and climate have a long history. As computer technology improves, models have been run at increasingly fine spatial resolution. A recent review by Simmons and Hollingsworth [1] shows that the increased resolution has had a positive effect on operational forecasting.

For climate problems involving long integrations, most studies even today are restricted to horizontal resolutions of ~T40–T60 (equivalent to grid spacing of 200–300 km). In recent years there have been some attempts at relatively brief integrations of global models at fine resolution in order to study particular aspects of the general circulation. Hamilton et al. [2, 3, 4] studied aspects of the tropospheric and stratospheric circulation in control integrations of the GFDL “SKYHI” model with horizontal grid spacing as fine as 35 km. They showed in particular that many aspects of stratospheric circulation improved as the model resolution is increased. Also Hamilton and Hemler [5] reported that a tropical cyclone generated spontaneously in the 35 km-resolution model simulation over the Northwestern Pacific developed into a typhoon to the south of Japan with central pressure reaching as low as 906 hPa. Conaty et al. [6] recently reported improved structure and evolution of extratropical cyclones, fronts, jet streams and tropopause by increasing resolution in their atmospheric general circulation model.

In March, 2002, the Earth Simulator (ES) started its operation [7], which provided unprecedented computational capability. We have performed a set of mesoscale

---

* ***Corresponding author****: Dr. Wataru Ohfuchi, The Earth Simulator Center, Japan Agency for Marine-Earth Science and Technology, 3173–25 Showa-Machi, Kanazawa, Yokohama, Kanagawa 236-0001, Japan. E-mail: ohfuchi@jamstec.go.jp*

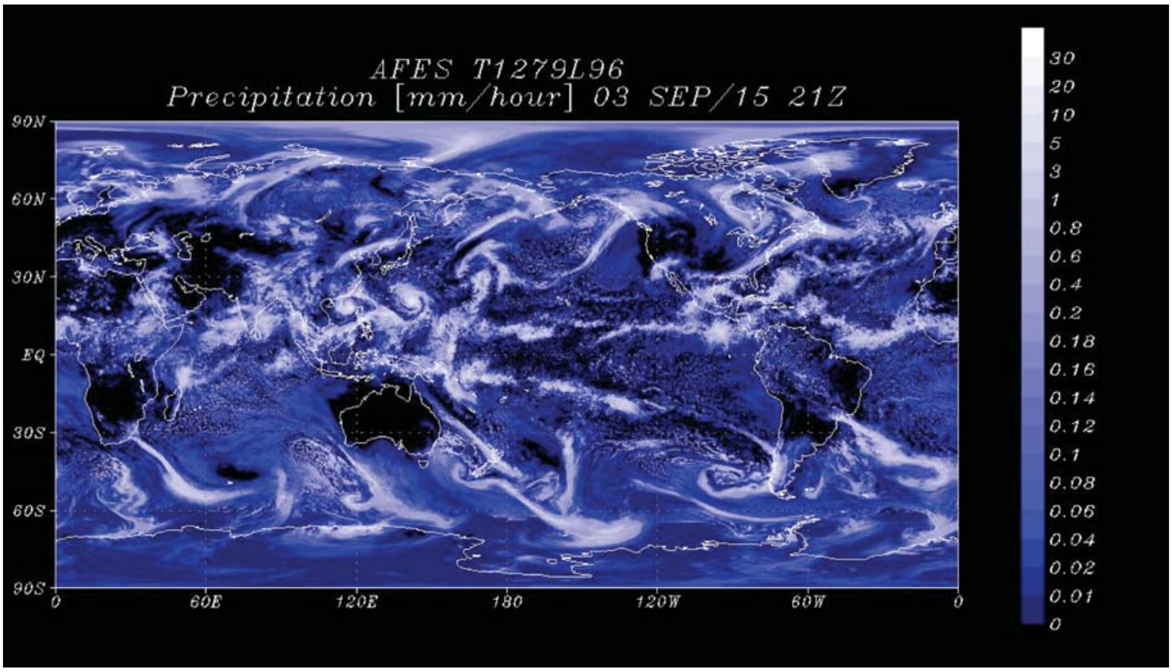

Fig. 1 An example of a global 3-hourly precipitation field.

resolving simulations of the global atmosphere with 10-km resolution. Here we report an overview of our effort in the experimental ultra-high resolution global atmospheric simulations. The ES is a gigantic parallel-vector computer manufactured by the Nippon Electronic Company (NEC), whose theoretical peak performance is 40 Tflops (i.e., $\sim 4 \times 10^{13}$ floating-point operations per second). In practice, the ES has achieved 35.86 Tflops for the LINPACK Test, a standard computational test of linear algebra. The ES is ranked as the world's fastest computer in the Top 500 List at the ISC2002 Conference in June, 2002. The ES is expected to remain the fastest computer until U.S. Department of Energy's Blue Gene/L (367 Tflops) and ASCI Purple (100 Tflops), both manufactured by IBM, start their full operation. The ES has also demonstrated its remarkable computational efficiency even for a realistic application in meteorology. We have been developing an atmospheric general circulation model (AGCM) that runs on the ES with extreme efficiency [8]. Our AGCM, called AFES (*A*GCM for the *ES*), has achieved 26.58 Tflops on the ES, for which it received the Gordon Bell Award for Peak Performance at the Super Computing 2002, held in Baltimore, MD, USA, November 2002 [8].

The high computational efficiency of AFES provides us with a unique opportunity to carry out mesoscale resolving simulations of the global atmosphere with horizontal resolution as high as 10 km. Though it does not necessarily improve every aspect automatically, higher resolution modeling should improve, for example, representation of mesoscale circulation systems and the effects of regional topography. Fig. 1 shows a global 6-hourly precipitation field from one of our 10-km mesh simulations. It is evident that the model can simulate not only large-scale features such as the intertropical convergence zone and mid-latitude baroclinic waves, but also mesoscale features such as typhoons. Our ultimate goal is a better understanding of atmospheric variability induced by interactions between large-scale fields and mesoscale phenomena.

For our first experiments, we focused on particular mesoscale phenomena: extratropical wintertime cyclogenesis over the North Pacific, the Baiu (Meiyu) frontal zone, and typhoon evolution. All of these are unique phenomena over East Asia and may significantly influence the weather and climate there. These phenomena were simulated in version of AFES with T1279 horizontal resolution and 96 levels in the vertical. This resolution allows the model to resolve mesoscale phenomena that previously could only be studied in regional models. Clearly a mesoscale resolving global model has an advantage in representing the feedback from meso-scale systems to the ambient flow. For example, mesoscale systems that accompany severe regional weather events are organized and developed locally in the course of a fast downstream development of a packet of baroclinic waves [9, 10]. A global model has an advantage in representing such a wave packet that propagates a great distance within a short period and in resolving the associated fast changes in the ambient flow structure for mesoscale systems.

A brief overview of the results of our global mesoscale-resolving simulation with AFES is presented in this paper, together with a description of AFES and the tuning strategies applied. More detailed analysis of interactions between larger scale circulations and mesoscale phenomena, and self-organization of meso-scale structures in larger scale circulations will be given in later papers.

2. Model description

The original code of AFES was adopted from the version 5.4.02 of an AGCM developed jointly by the Center for Climate System Research (CCSR) of the University of Tokyo and the Japanese National Institute for Environmental Sciences (NIES). The particular version of the CCSR/NIES AGCM has been used for several international modeling efforts, including future projections for the Intergovernmental Panel for Climate Change (IPCC; [11]) and Atmospheric Model Intercomparison Project (AMIP; [12]).

As for the CCSR/NIES AGCM, AFES is based on the primitive equation system under the hydrostatic approximation. The governing equations are written in the vorticity-divergence form [13] with the spectral Eulerian advection scheme. The semi-implicit method is used for the time integration. In the dynamical core of AFES, the spectral transform method is used for horizontal discretization [14] and the Lorenz differencing method in the vertical σ-coordinate [15]. AFES is a full AGCM with the same physics parameterization package as in the version 5.4.02 of the CCSR/NIES AGCM [16]. The package includes an accurate radiative transfer scheme developed by Nakajima and Tanaka [17], a simplified Arakawa-Schubert convective scheme [18] with a crude treatment of the effect of convective downdraft, and Mellor-Yamada level-2 vertical diffusion scheme [19]. The performance of AFES as a global climate model has recently been verified at moderate horizontal resolution (e.g., [20]).

The mesoscale resolving AFES simulations of the global atmosphere described below were conducted with horizontal resolution of the triangular truncation at wavenumber 1279 (T1279) or equivalently about 10-km grid intervals. The model has 96 vertical levels with the top level placed at about $\sigma = 0.001$ (about 1 hPa). The layer thickness varies from 20 m near the surface to about 500 m in the mid-troposphere through the mid-stratosphere. The 10-km grid size, with which mesoscale features as small as 30–40 km in size can probably be resolved, is very close to the smallest scale in which the hydrostatic approximation used in the primitive equation system is valid. One may consider that a grid interval of 10–20 km may be unnecessarily high for a hydrostatic simulation with a parameterized cumulus convection. Though unable to resolve individual cumulus clouds, such a small grid interval as 10–20 km is necessary to represent "mesoscale convective systems" (e.g., [21, 22]), including spiral rainbands and eyewall clouds of a tropical cyclone or frontal rainbands that are organized under a synoptic and meso-α-scale flow with the effect of self-induced convective downdraft and surface friction. In fact, as discussed later, most of the heavy precipitation simulated at such a high resolution arises from grid-scale condensation, indicating that, though maybe in a somewhat distorted manner, our global model can resolve regional organization of such mesoscale convective systems.

The original code of the CCSR/NIES AGCM [16] was written in FORTRAN 77 and unparallelized. In pursuit of the highest computational efficiency on the ES, the code has been totally rewritten for AFES into FORTRAN 90 with the adaptation of the Message Passing Interface (MPI). Specifically, hybrid programming is employed for taking the full advantage of three-level parallelization available on the ES [8]. The parallelization includes (i) inter-node parallel processing for distributed memory architecture by utilizing the MPI library, (ii) intra-node parallel processing for shared memory architecture within each node by utilizing microtasking (a kind of thread programming), and (iii) vector processing for the vectorized architecture in a single processor. For these three levels of parallelization, the maximum numbers of parallel decomposition are 640, 8, and 256, respectively. They correspond to the total number of nodes on the ES, the number of processors within a node, and the number of vector register elements within a processor, respectively. Furthermore, AFES code has been optimized to take full advantage of the high-speed Interconnection Network on the ES that consists of single-stage full crossbar switches (with the transmission speed of 12.3GB $s^{-1} \times 2$). Specifically, the combination of one-sided communication facilities of MPI-2, MPI_PUT and MPI_WIN_FENCE, is implemented in AFES dynamical core for data transpose communication for the spectral transform scheme. AFES also utilizes the Global Memory System, which is a new type of a shared memory system for multiple processes working on distributed computational nodes of the ES. The system, known as the "zero copy" system, allows data communication without performing an excessive memory copy with a system buffer.

The time step interval is varied in the course of the model integration, to meet the Courant-Friedrich-Levy (CFL) condition at every time step. An interval of about 15 seconds is required for stable numerical integration with the T1279 resolution. As the computational burden for the Legendre transform (LT) in a spectral model increases with the third power of the truncation wavenumber, the LT accounts for the largest fraction of the total elapsed time for an AFES simulation with the T1279 resolution. Yet, owing to its optimized coding for the LT, AFES has achieved a remarkable computational performance with very high vector efficiency and excellent scalability even at the T1279 resolution. In fact, the LT process accounts for less than 60% of the total elapsed time for a T1279 simulation.

3. Simulations

Each of our T1279L96 AFES simulations was conducted for an integration period of 10 or 16 days, as an extension of a long-term simulation at T319L24 resolution (equivalently, 40-km horizontal mesh and 2000-m layer thickness from the mid-troposphere to the mid-stratosphere). The initial condition for the T319L24 simulation was taken from the global field for 0000 UTC on January 1, 1979 based on the NCEP (National Centers for Environmental Prediction)/ NCAR (National Center for Atmospheric Research) reanalysis data [23]. It should be stressed that it is not a hindcast experiment that targets a specific weather event actually observed. Rather, it is a purely experimental simulation in which we attempt to resolve some typical mesoscale phenomena in a realistic manner under the climatological boundary condition. As the initial condition for each of the T1279 integrations, we selected a particular snapshot in the T319L24 integration about five days before the full development of a particular mesoscale feature of interest. Table 1 summarizes the starting dates and the durations of simulations of the T1279L96 simulations taken from the 12-year T319L24 simulation. After initialization from the T319L24 fields, finer-scale features develop in the finer resolution model within a couple of days.

As the model boundary condition, daily fields of climatological-mean sea-surface temperature (SST) and sea-ice cover were linearly interpolated from monthly fields of the Hadley Centre Ice and SST (HadISST) climatology (Rayner et al. [24]; available online at http://dss.ucar.edu/datasets/ds277.3). The surface topography and surface characterization were based on the Global 30 Arc-Second Elevation (GTOPO30) and Global Land Cover Characterization (GLCC) data sets, respectively. These datasets are distributed by the Land Processes Distributed Active Archive Center (LP DAAC) in the U.S. Geological Survey's EROS Data Center (available online at http://edcdaac.usgs.gov). Spectral filtering was applied to the topography data, since suppressing the very high wavenumber components of the topography is necessary for stable numerical integration at the T1279 resolution. The monthly mean atmospheric ozone climatology used in our simulations was constructed from the data provided by Drs. Liang and Wang of the Atmospheric Sciences Research Center, State University of New York at Albany (http://www-pcmdi.llnl.gov/amip/AMIP2EXPDSN/OZONE/OZONE2/o3wangdoc.html).

4. Results

4.1. Wintertime cyclogenesis

Since the pioneering works by Gall [25] and Simmons and Hoskins [26], numerous experiments with hemispheric or global models have been performed to study the evolution, structure and dynamics of extratropical cyclones. AGCMs with spectral resolution of T42 or T63 that are now commonly used for climate studies are capable of resolving synoptic features of individual extratropical cyclones. Moreover, those models can reproduce some key statistics of their ensemble behavior reasonably well, including subweekly wind fluctuations and associated poleward fluxes of heat and vorticity that characterize so-called "midlatitude storm tracks" (e.g., [27, 28]). However, the resolution of such AGCMs is not high enough to resolve fine structures observed with developing cyclones, such as sharp cross-frontal thermal contrasts, frontal rainbands and mesoscale convection behind a cold front. Recent field observations have revealed other fine structures that are not in the classical picture of the Bergen School model of frontal cyclones [29, 30]. Those features, including frontal fracture and warm-core seclusion in the proximity of the mature cyclone center, have been reproduced realistically in hindcast experiments with regional mesoscale models [31], but they are unlikely to be resolved in the global AGCMs currently available. Nowadays, modern, state-of-the-art global forecast models with T213 or somewhat higher spectral resolution that are in operation at several forecast centers can simulate fine PV structure at the tropopause level associated with mature baroclinic waves, including wrap-up of high-PV filaments within a deepened upper-level trough (e.g., [32]). We will show, below, that those fine mesoscale frontal structures and upper-level PV filaments associated with an extratropical cyclone appear in an

Table 1 Starting dates of the T1279L96 simulations from the 12-year T319L24 simulation.

Numerical Experiment	Start Date	Length of Simulations
Wintertime Cyclogenesis Experiment	0 UTC, January 7, 0002	10 days
Baiu (Meiyu) Frontal Zone Experiment	0 UTC, June 21, 0001	10 days
Typhoon Genesis Experiment	0 UTC, September 6, 0003	16 days

AFES simulation. We will show another example of the same simulation, in which rainbands and topographic precipitation associated with a surface "polar low" and a cold vortex aloft developed around Japan are simulated in a fairly realistic manner.

4.1.1. MATURE CYCLONE IN THE NORTH PACIFIC

As our first example, we show the three-dimensional structure of a mature extratropical cyclone over the central North Pacific simulated by T1279L96 AFES integration (Fig. 2). The cyclone is initiated on the second day of the integration just to the east of Japan with the sea-level pressure (SLP) at the storm center of 1000 hPa. For the next two days the storm undergoes explosive development, until it matures to the south of the Aleutian Islands with the central pressure as low as 954 hPa (Fig. 2a). Sequential maps of upper-level meridional wind anomalies in Fig. 3 suggest that the particular cyclogenesis occurs locally within a core of the Pacific jet, without significant downstream influence of a fast-propagating baroclinic wave packet, although a packet arriving at its mature stage seemingly acts to maintain the low. The explosive growth occurs in the exit of the jet well to the north of the axis.

The storm system exhibits a familiar looking precipitation pattern (Fig. 2a), as often seen in satellite cloud imagery in association with a developed extratropical cyclone (e.g., Fig. 10.22 of Shapiro and Keyser [29]). The organized precipitation pattern is in good correspondence

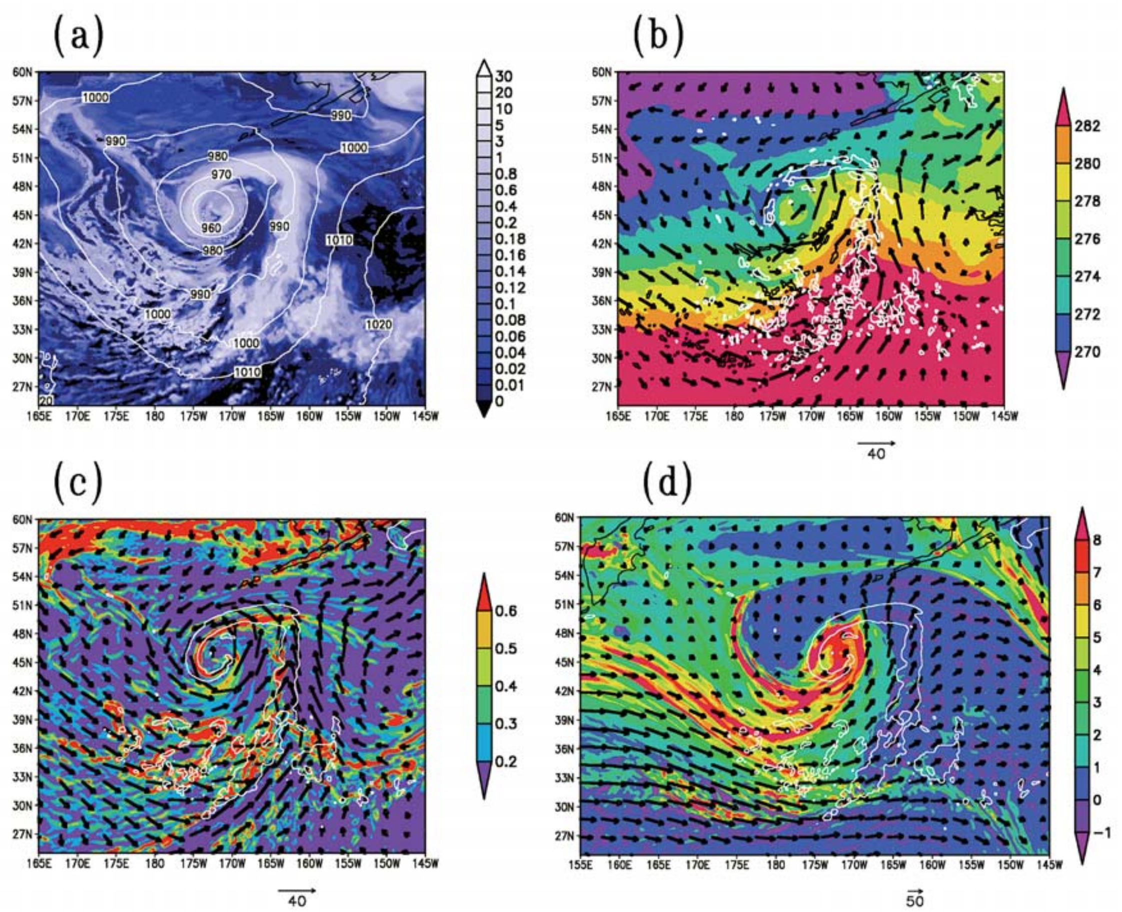

Fig. 2 Snapshot of a mature synoptic-scale cyclone over the central North Pacific simulated on the fourth day of a T1279L96 AFES integration (1200 UTC, 10 January). (a) Sea-level pressure (white contours: every 10 hPa) and precipitation rate (with color convention indicated at the right; Unit: mm h^{-1}). (b) Mid-tropospheric vertical motion (P-velocity ω at the $\sigma = 0.5$ level; white contours: ascent of $\omega = -1.0$ Pa s^{-1}; black contours: descent of $\omega = +1.0$ Pa s^{-1}), superimposed on near-surface fields of horizontal wind (arrows with scaling at the bottom; Unit: m s^{-1}) and air temperature (with coloring convention at the right; Unit: K) both at the level of $\sigma = 0.95$. (c) Precipitation rate (white contours: 1 mm h^{-1}), superimposed on near-surface fields of horizontal wind (arrows with scaling at the bottom; Unit: m s^{-1}) and horizontal temperature gradient (with color bar at the right; Unit: K 10^{-1} km) both at the level of $\sigma = 0.95$. (d) Precipitation rate (white contours: 1 mm h^{-1}), superimposed on upper-tropospheric fields of horizontal wind (arrows with scaling at the right; Unit: m s^{-1}) and Ertel PV (σ-level version; with color bar at the bottom; Unit: PVU) both at the level of $\sigma = 0.3$. Note that the zonal extent of panel (d) is wider than that of the other panels.

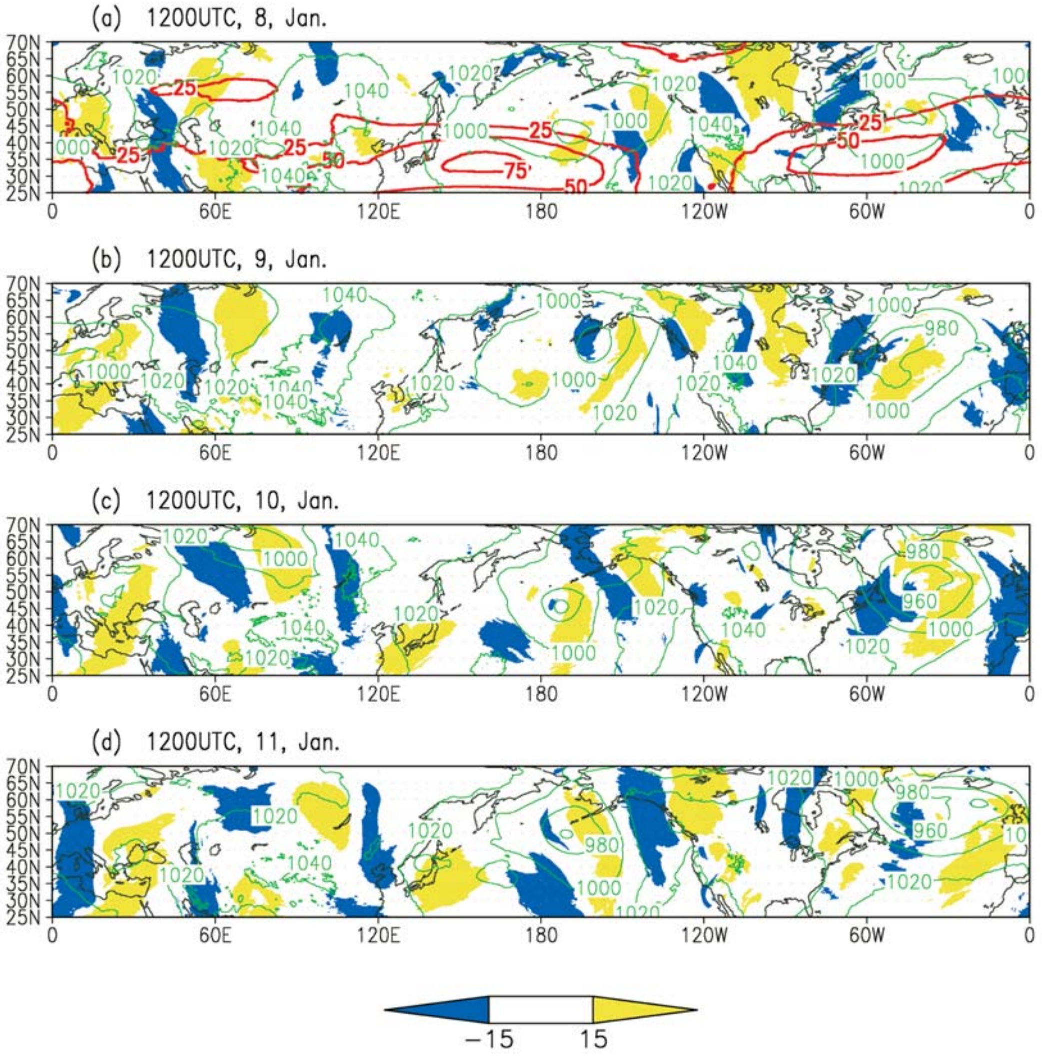

Fig. 3 Maps of anomalous meridional wind velocity (yellow: the southerlies stronger than 15 m s^{-1}; blue: the northerlies stronger than 15 m s^{-1}) at the level of $\sigma = 0.3$ for the second (a), third (b), fourth (c) and fifth (d) days (top to bottom) of a T1279 AFES integration (at 1200 UTC on the 8, 9, 10 and 11-th days of January, respectively). The meridional wind anomalies that are defined locally as instantaneous local departures from the time mean field over the first 10 days of the integration emphasize daily wind fluctuations associated with migrating synoptic-scale disturbances. The corresponding instantaneous SLP fields (every 20 hPa) are superimposed with green contours. Red lines in the upper panel represent the 10-day mean westerly wind speed (25, 50 and 75 m s^{-1}) at the $\sigma = 0.3$ level.

with the surface fronts (Fig. 2c), including a continuous sharp front that corresponds to an occluded front in the classical Norwegian cyclone model [33]. Precipitation is also pronounced along, but slightly ahead of, a surface cold front, whereas the signature of a classical warm front is rather weak with respect to precipitation and the near-surface thermal contrast. The entire frontal structure and associated precipitation pattern bear certain resemblance to the "frontal T-bone" suggested in Shapiro's cyclone model [29, 31, 30]. In fact, the meridional section across the surface cyclone center (Fig. 4b) indicates that the zonally-oriented front north of the cyclone center is rather shallow and inclined gradually poleward with height, without showing any indication of merging of a cold front aloft. The front accompanies a low-level easterly jet that corresponds to a "cold conveyor belt" [34, 35, 36]. These are the characteristics of a "bent-back warm front" in Shapiro's model (based on recent observations of intensified marine cyclones).

In the lower troposphere, the cyclone center is located within a region of relatively warm and humid air with diameter of ~300 km, secluded almost completely from the surrounding cooler air by the bent-back front (Figs. 2 and 4). To the west and south of the warm cyclone core, the particular front is deeper than to the north of the core, exhibiting stronger resemblance to a cold front. This deep

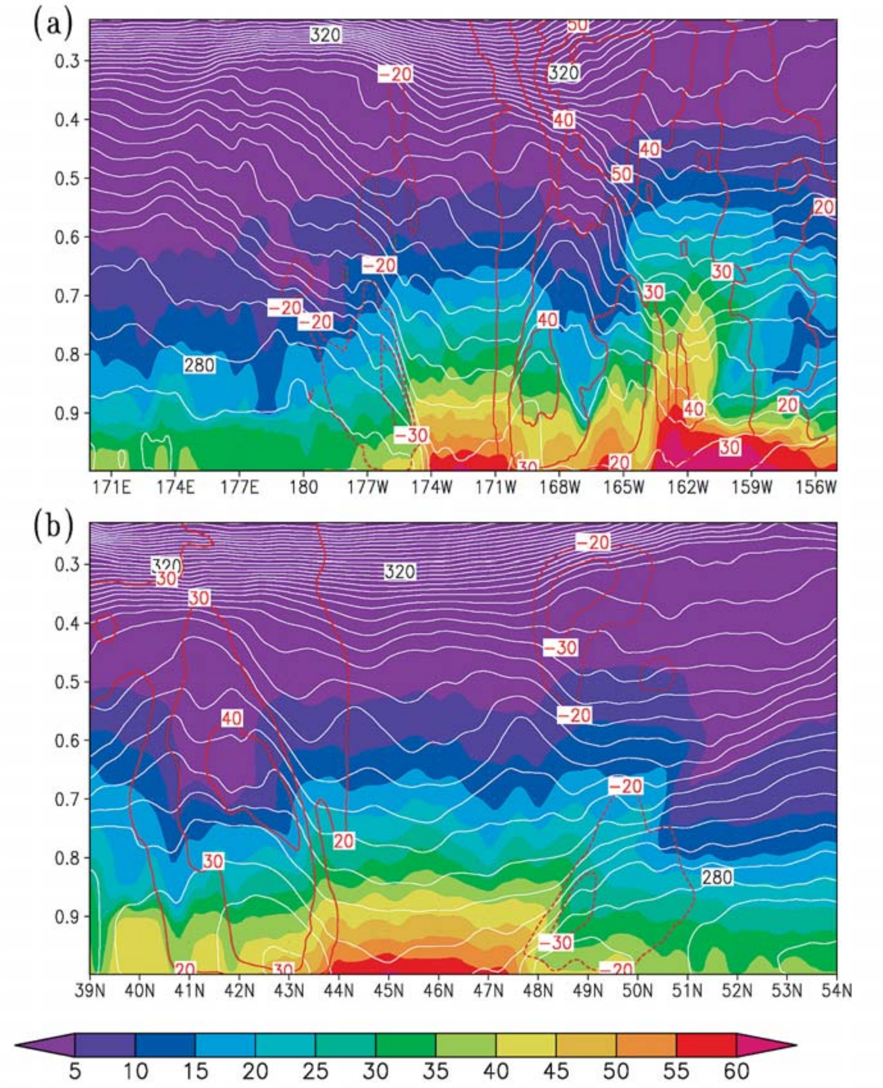

Fig. 4 (a) Zonal section of potential temperature (every 2 K with white lines) and specific humidity (with coloring convention at the bottom: unit: 0.1 g kg^{-1}) across the surface cyclone center (45°N, 172.5°W) for 1200 UTC of the fourth day of a T1279 AFES integration. Meridional winds (m s^{-1}) are indicated with red lines (every 10 from 20; negative for the northerlies). (b) As in (a), but for meridional section across the cyclone center. Zonal winds (m s^{-1}) are indicated with red lines (every 10 from 20; negative for the easterlies).

frontal spiral is associated with high-PV filaments at the tropopause level wrapping up cyclonically within the deepened upper-level trough (Fig. 2d). Along this deep frontal surface, extremely dry air appears to be intruding downward from the stratosphere (Fig. 4), indicative of the occurrence of tropopause folding [37]. Below one of the high-PV filaments, a belt of particularly strong mid-tropospheric subsidence of relatively warm but extremely dry air extends almost zonally at ~42°N along the mid-tropospheric westerlies formed to the immediate south of the southward-tilting frontal surface (Fig. 4b). This is indicative of dry-air intrusion (or a “dry slot” in satellite imagery) associated with an upper-level jet streak, as typically observed right behind an intensified surface cyclone [38, 35, 36]. Tropopause folding also occurs right behind the main cold front as typically observed (Fig. 4a). Though less pronounced, there seem to be a few other indications of tropopause folding in the cross sections of Fig. 4. At this stage we are not certain whether they really indicate a local fold of the tropopause associated with gravity waves.

At the surface the main cold front extending meridionally at 164°W is “fractured” at many locations (Fig. 2c). With the most distinct “discontinuity” (i.e., weakening of the thermal contrast) found at its northern end, the cold front appears to be disconnected from the bent-back front,

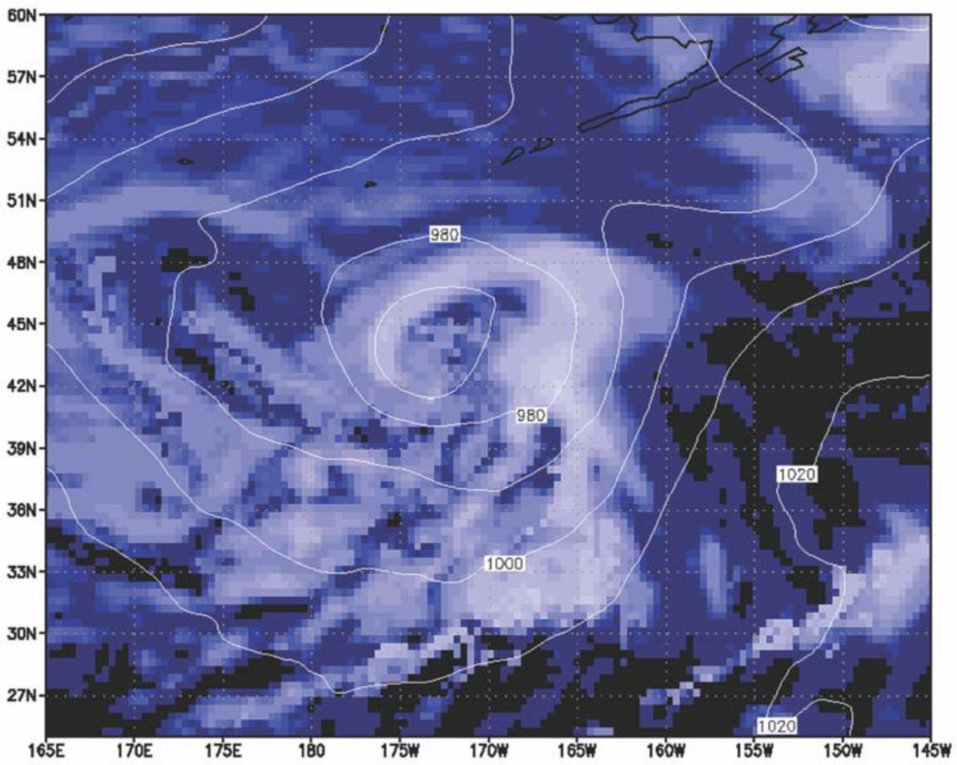

Fig. 5 As in Fig. 2a, but for the counterpart in the T319L48 AFES integration.

which corresponds to the "frontal fracture" in Shapiro's model. An intense southerly jet is formed in the lower troposphere right ahead of the main cold front (Fig. 4a), accompanying a pronounced mid-tropospheric ascent (Fig. 2b). This ascending airstream that transports warm, moist air poleward is regarded as the "warm conveyor belt" [35, 36]. Along the cold front, the associated precipitation pattern also seems to be "fractured", reminiscent of mesoscale convective rainbands observed within the warm conveyor belt [39]. The overall evolution of the surface frontal structure and upper-tropospheric PV (Fig. 2) suggests that the particular cyclone simulated in the model may be classified into the "Life Cycle 1 (LC1)" case [40], a cyclone development in the westerlies with only weak barotropic shear.

In addition to the realistic mesoscale features as a part of the frontal structure of the cyclone, AFES can also simulate mesoscale precipitation systems within cold air spreading behind the main cold front (Fig. 2a). Those precipitation systems that are considered stratocumulus type tend to be lining up in parallel to the near-surface westerlies, and those with heavy precipitation accompany strong localized ascent (Fig. 2b). One of those convective systems, located to the south of the main storm center, is about to organize itself into a mesoscale disturbance with a comma-shape precipitation pattern.

The T319L24 integration can reproduce gross features of the particular synoptic cyclone including the "frontal T-bone" (Fig. 5). However, the cyclone is weaker (with central pressure ~20 hPa higher) than its counterpart in the T1279 integration. The thermal contrast across the main cold front is somewhat reduced, and the wrap-up of the bent-back front near the cyclone core is less apparent. Furthermore, mesoscale precipitation is weaker and less organized within cold air behind the main cold front.

4.1.2. POLAR LOW AND TOPOGRAPHIC PRECIPITATION

As our second example, we show the evolution of a polar low simulated over the Far East in the T1279L96 AFES integration. In Fig. 6a for the fifth day of the model integration (11 January), the low is recognized as a near-surface cyclonic vortex with a spiral precipitation pattern over the Sea of Japan, as sometimes observed [41, 42]. The low develops in association with the amplification of the Siberian High and a subsequent large-scale cold-air outbreak from the Asian continent. The cold air spreads widely over the Northwestern Pacific, extending as far south as the Philippines and Indochina Peninsula. After being modified by heat supply from the warm ocean surface, the near-surface northerlies from the continent are converging near the Mindanao and Borneo Islands, where particularly heavy convective precipitation is organized. No organized pattern of precipitation was found over the Sea of Japan 36 hours earlier (Fig. 6b), indicative of the rapid development of the low.

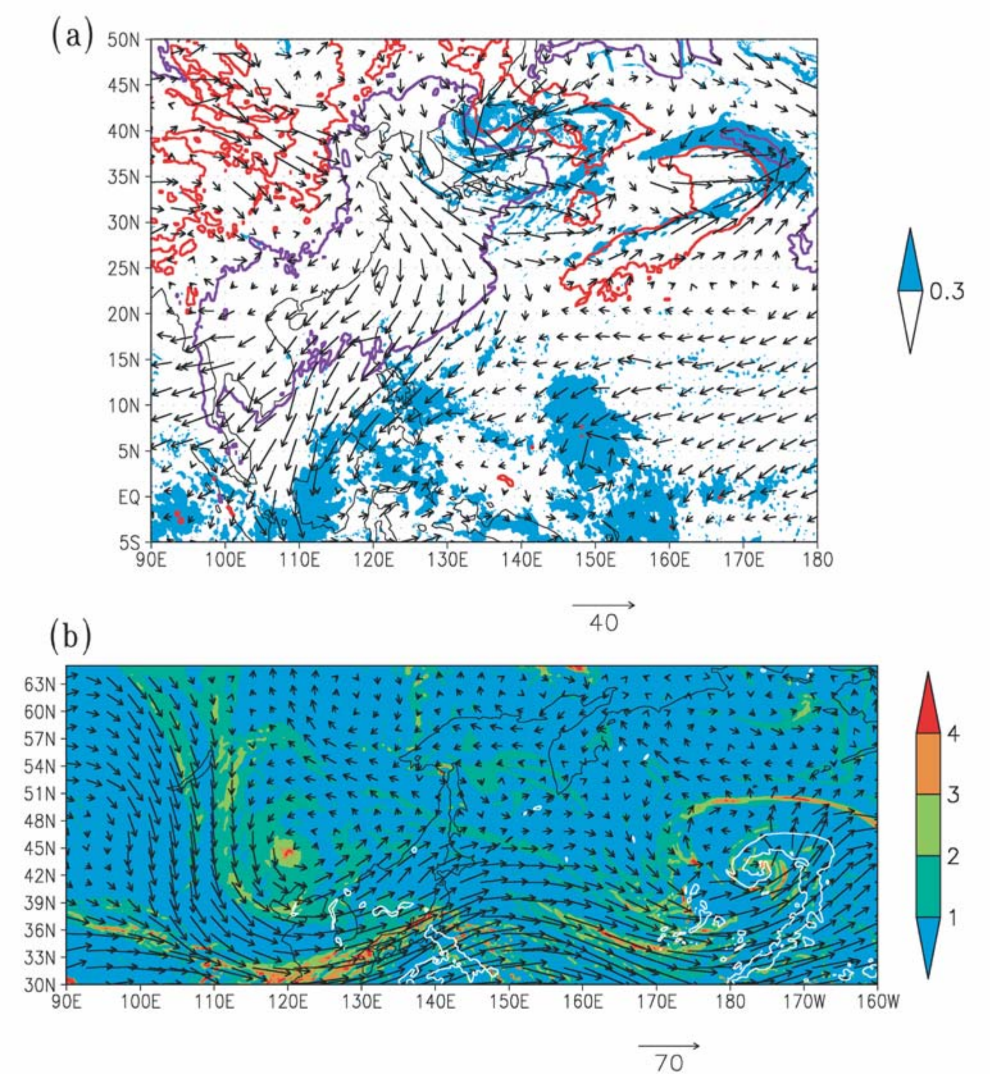

Fig. 6 (a) Near-surface wind (arrows with scaling at the bottom: unit: m s^{-1}) and anomalous temperature (red contours: +2 K; purple contours: –2 K) at the level of $\sigma = 0.95$ for 1500 UTC of the fifth day of a T1279 AFES integration. The anomalies are defined locally as instantaneous local departures from the time mean field over the first 10 days of the model integration. Precipitation stronger than 0.3 (mm h^{-1}) is superimposed with blue shade. (b) Horizontal winds (arrows with scaling at the bottom; unit: m s^{-1}) and Ertel potential vorticity (with color convention indicated at the right; unit: PVU) defined at the level of $\sigma = 0.5$ for 0300 UTC of the fourth day of a T1279 AFES integration. Precipitation with rate of 1 (mm h^{-1}) is superimposed with white contours.

The polar-low development followed synoptic-scale cyclogenesis east of Japan, which occurred upstream of the mature cyclone over the central North Pacific we discussed previously (as seen near the lower-right corner of Fig. 6b). In contrast to the observed typical evolution of a polar low [43, 44, 41], the “parent low” to the east does not strongly amplify in this particular case. Rather, the marked deepening of an upper-level trough over the Far East (Fig. 6b) and the presence of the sharp thermal contrast underneath between the Asian continent and the Sea of Japan (Fig. 7a) are considered crucial in the rapid development of this particular low (c.f., [41]). The near-surface baroclinicity is also strong locally in the southern part of the Sea (Fig. 7a), where a zonally oriented precipitation band is formed (Fig. 6b). At this stage (0300UTC, January 10), the surface cold air is mostly confined within the continent (Fig. 7a). The upper-level trough is deepening just downstream of a strong ridge over Mongolia. In between, the pronounced cyclonic shear along the strong northerlies forms itself into a high-PV filament wrapping up into the high-PV core within the trough. It is suggested that the anomalously high PV within the trough acts to induce anomalous warm advection across the surface baroclinic zone over the Sea of Japan.

Within the next 18 hours, the polar low with the surface central pressure of 998 hPa develops over the west-

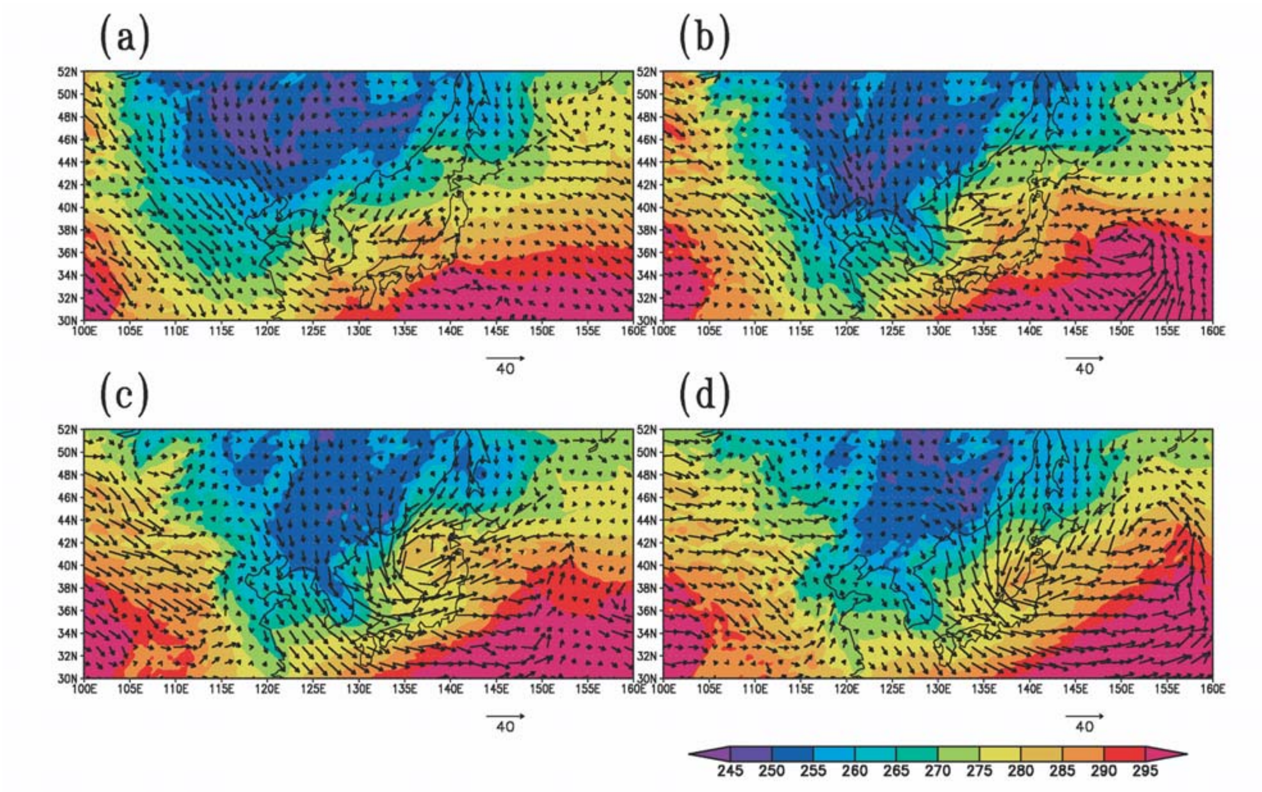

Fig. 7 Snapshots of near-surface wind (arrows with scaling at the bottom: unit: m s^{-1}) and equivalent potential temperature (with color bar at the bottom; unit: K) at the level of $\sigma = 0.95$ associated with a polar low over the Sea of Japan in a T1279L96 AFES integration for (a) 0300 UTC of the fourth day (10 January), (b) 2100 UTC of the fourth day, (c) 1500 UTC of the fifth day (10 January) and (d) 0300 UTC of the sixth day (12 January) of the model integration.

ern part of the Sea of Japan (Fig. 8a). From the cyclone center a well-defined precipitation band extends southeastward, to which warm, moist air is converging near the surface (Fig. 8b). Along this convergence zone, part of that warm air appears to be advected toward the cyclone center, at which a tiny warm core is present with its zonal extent less than 50 km (Fig. 7b). The thermal contrast is not particularly strong across the convergence zone. The contrast is more profound behind the surface low, where a strong outbreak of cold continent air occurs over the warm sea surface under the tight SLP gradient. Under this condition, convective precipitation behind the low is organized into several narrow bands lining up nearly in parallel to the local surface wind. Precipitation is particularly enhanced along another convergence zone that forms downstream of the North Korean mountain range, as observed [45]. The upper-level trough starts breaking cyclonically (Fig. 9a), as observed in a pronounced cold-air outbreak over the Far East [46], with the enhanced wrap-up of the high-PV filament. The high-PV core is still situated upstream of the surface low, contributing to the baroclinic growth of the low.

The polar low attains its full intensity within the next 12 hours. The center has deepened as low as 986 hPa (Fig. 8b). Precipitation now spreads almost entirely over the Sea of Japan (Fig. 8b), except within the warm cyclone core and poleward of the zonally oriented convergence zone to its south (Fig. 7c). The weak gradient of near-surface equivalent potential temperature (θ_e) across the zone exhibits a sharp contrast with tight θ_e gradient across a synoptic cold front to the south of Japan. Rather, the convergence zone coincides with local θ_e maxima, which favors heavy convective precipitation. Between this zone and the cold front to the south, precipitation bands are oriented along the prevailing westerly or northwesterly winds. Precipitation is also heavy along another convergence zone that extends eastward to the north of the storm over relatively warm, moist air at the surface. Another band of heavy precipitation oriented meridionally behind the low exhibits more front-like structure with enhanced θ_e gradient. In the mid-troposphere (Fig. 9b), the trough has undergone further deepening, while suffering from strong deformation by the cyclonic shear associated with the intensified subtropical jet. Thus breaking cyclonically, the high-PV air within the trough is stretched eastward and its tip is wrapping up into a mesoscale cyclonic vortex right over the surface polar low. The mature low has now become barotropic, and its baroclinic growth has ceased.

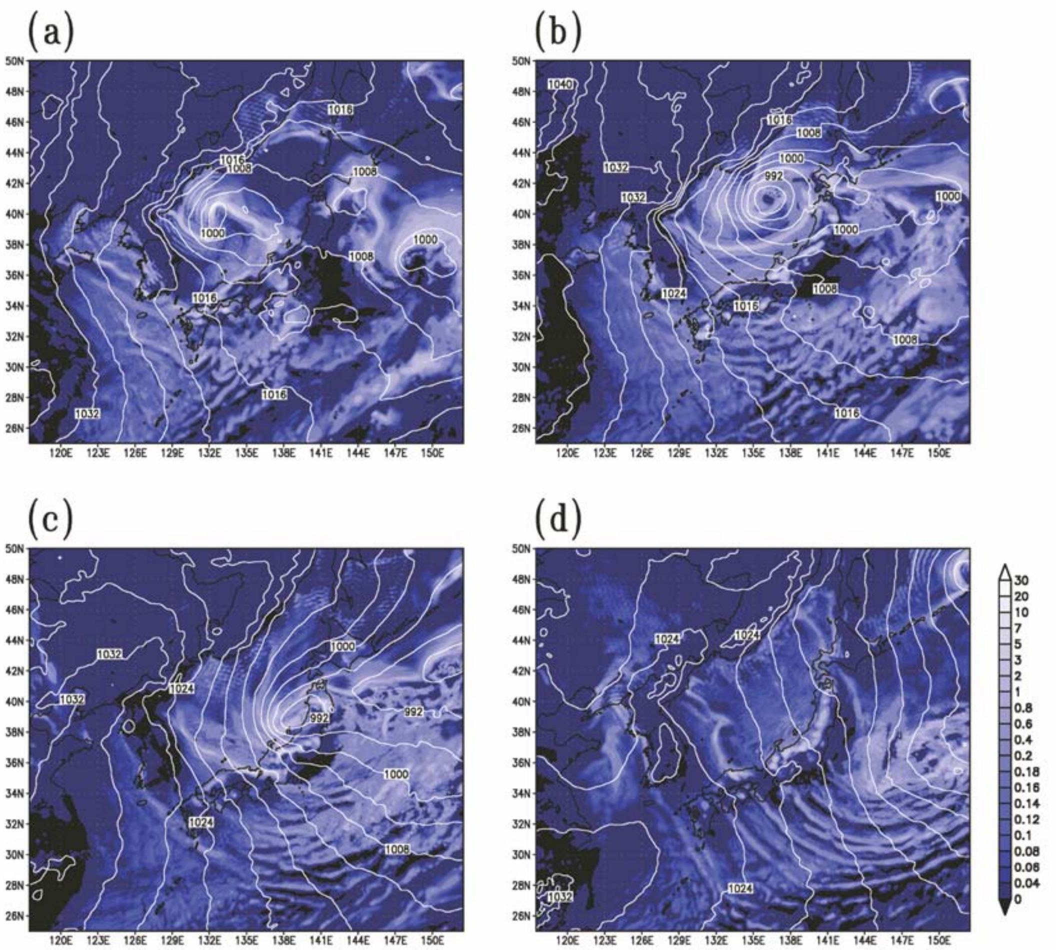

Fig. 8 Snapshots of sea-level pressure (white contours: every 10 mb) and precipitation rate (with color bar at the lower right; unit: mm h^{-1}) associated with a polar low over the Sea of Japan in a T1279L96 AFES integration for (a) 2100 UTC of the fourth day (10 January), (b) 1500 UTC of the fifth day (10 January), (c) 0300 UTC of the sixth day (12 January) and (d) 1800 UTC of the sixth day of the model integration.

Within the next 12 hours (0300 UTC, January 12), the polar low starts decaying while migrating southeastward (Fig. 8c). Yet, precipitation is still heavy along the convergence zone that originated off the North Korean coast and that now extends southeastward. In the mid-troposphere (Fig. 9c), the high-PV air within the trough has been further stretched eastward under the cyclonic shear of the subtropical jet. To the immediate north of the high-PV air, low-PV air is intruding westward under the cyclonic breaking, resulting in the reversal of meridional PV gradient. The surface polar low is now situated below the breaking low-PV air. By 1800 UTC, January 12, the polar low has completely diminished, leaving its remnant as a cluster of precipitating clouds off the east coast of Japan (Fig. 8d).

The rapid development of the particular polar low seems attributable in part to the deepening of the upper-level trough over the Far East and its interaction with the sharp thermal contrast between the Asian continent and the Sea of Japan. The deepening appears to be associated with an incoming (baroclinic) wave packet across the Eurasian continent with eastward group velocity of 35–40 m s^{-1} (Fig. 3). The amplification of the surface low is also attributable to strong upward motion associated with mesoscale convective precipitation in and around of its warm core. Seemingly, the rapid decay of the low arises from the termination of its baroclinic growth resulted from the shear stretching and cyclonic breaking of the upper-level trough. Neither a regional model alone nor a lower resolution AGCM alone could resolve all of these processes among others that characterize the time evolution of the particular polar low simulated in AFES. Furthermore, any other AGCM currently available is unlikely to simulate the organized mesoscale precipitation systems associated with polar-low development and cold-air outbreaks as realistically as T1279 AFES can. Even its counterpart in the T319 AFES integration is much weaker and the associated precipitation pattern

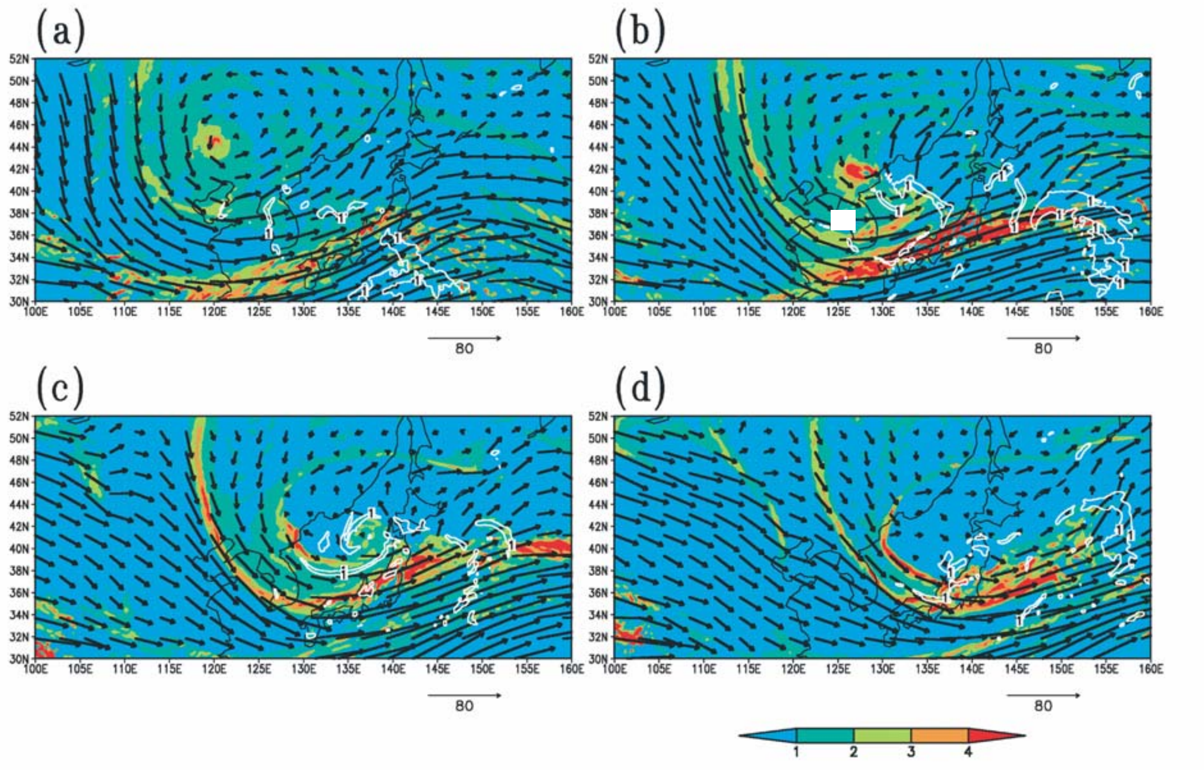

Fig. 9 As in Fig. 7, but for horizontal winds (arrows with scaling at the bottom; unit: m s^{-1}) and Ertel potential vorticity (with coloring convention indicated at the bottom right; unit: PVU) defined at the level of $\sigma = 0.5$. Precipitation with rate of 1 (mm h^{-1}) is superimposed with white lines.

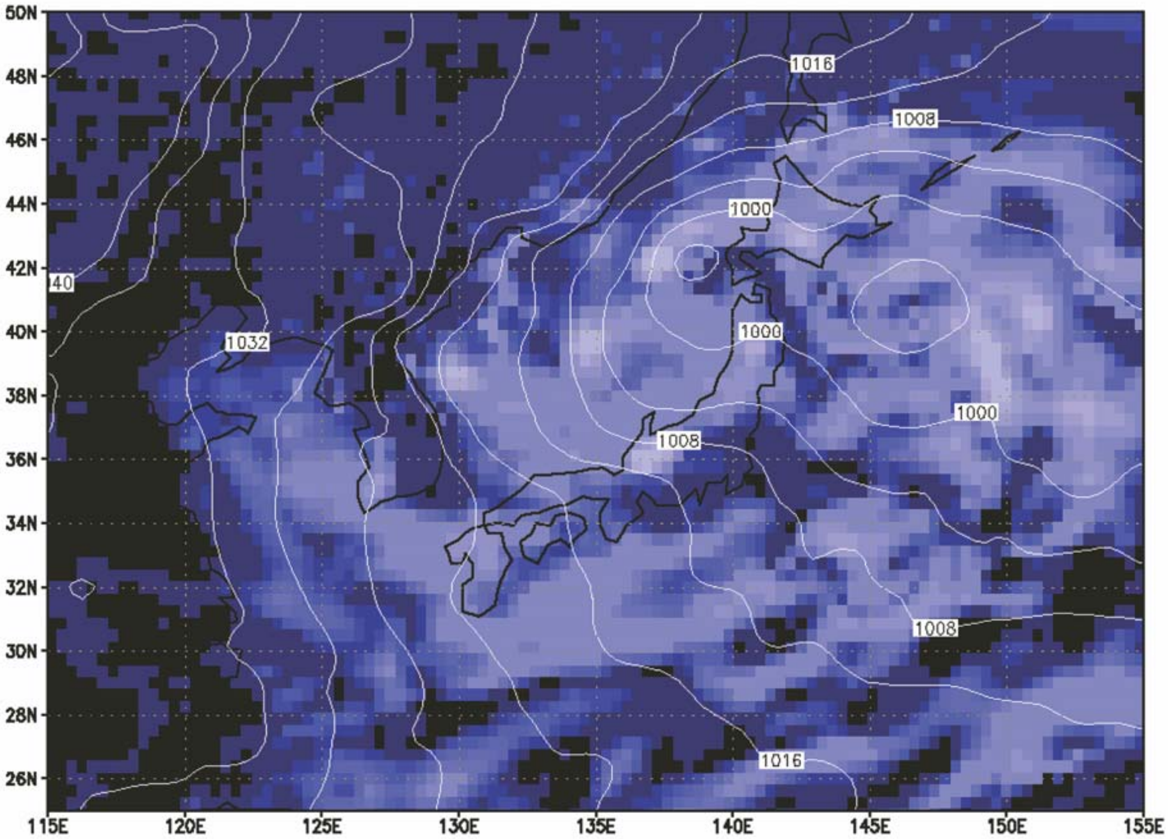

Fig. 10 As in Fig. 8b, but for the counterpart in the T319L48 AFES integration.

seems much less organized (Fig. 10).

In addition, the T1279 AFES integration can reproduce topographic precipitation and associated “rain shadow” in a fairly realistic manner. The low-level westerlies or northwesterlies prevailing south of the polar low carry a cold, dry continental airmass (Figs. 7a–c), to which abundant supply of heat and moisture occurs from the warm Tsushima Current and the Kuroshio. As observed typically in winter, the moistened low-level winds produce heavy precipitation as they reach the windward slopes of mountain ranges in Honshu Island of Japan (Figs. 8a–c). At 0300 UTC, January 12 (Fig. 8c), the topographic precipitation is particularly enhanced locally in a windward coastal region of Honshu, where the convergence zone extending southeastward from the North Korean coast reaches. Such landing of the convergence zone as simulated in Fig. 8c is known to yield extraordinarily heavy snowfall in a particular region on the west coast of Honshu in winter. In sharp contrast, simulated precipitation is much less along the Pacific coast of Japan on the lee of the mountains of Honshu, Kyushu and Shikoku Islands (Fig. 8), which is also in good agreement with the observation. Figs. 8b and c show that the Kanto Plain, which includes the urban and suburban areas of Tokyo, is under the complete “rain shadow” of the central mountain range of Honshu, as often observed in winter. Under a more typical monsoonal SLP pattern that emerges after the polar low has moved across Japan (Fig. 8d), heavy precipitation prevails almost entirely along the west coast of Japan, which is in sharp contrast with mostly dry condition prevailing along its Pacific coast. In Fig. 8d, one can recognize three bands of heavy precipitation that extend over the Kuroshio from immediately off the coast. A close inspection reveals that they are, from west to east, originated in the Bungo Straight (between Kyushu and Shikoku), Kii Straight (between Shikoku and the Kii Peninsula) and Ise Bay (east of the Kii Peninsula), respectively, as often seen in satellite imagery. Blowing down over one of these straits or the bay, the monsoonal northwesterlies can blow across the landmass of Japan with the shortest distance without being blocked by high mountains. These localized precipitation bands over those water paths are as narrow as 30–50 km in width and could not be reproduced in any AGCM until the advent of AFES on the ES. Even in the T319 integration, those bands are simulated in a more diffusive manner (Fig. 10). With less smoothed topography imposed, the improved version of AFES will be able to simulate even finer features of topographic precipitation in any region over the globe.

4.2. Baiu (Meiyu) frontal zone

The Baiu (Meiyu) frontal zone (BFZ) is composed of meteorological phenomena at a wide range of scales [47]. The BFZ, as a whole, is a part of the Asian summer monsoon system (Fig. 11a). Cyclonic disturbances with synoptic, sub-synoptic and meso-α-scales migrate along the BFZ (Fig. 11b). Individual meso-α-scale cyclones include meso-β-scale convective ensembles as internal

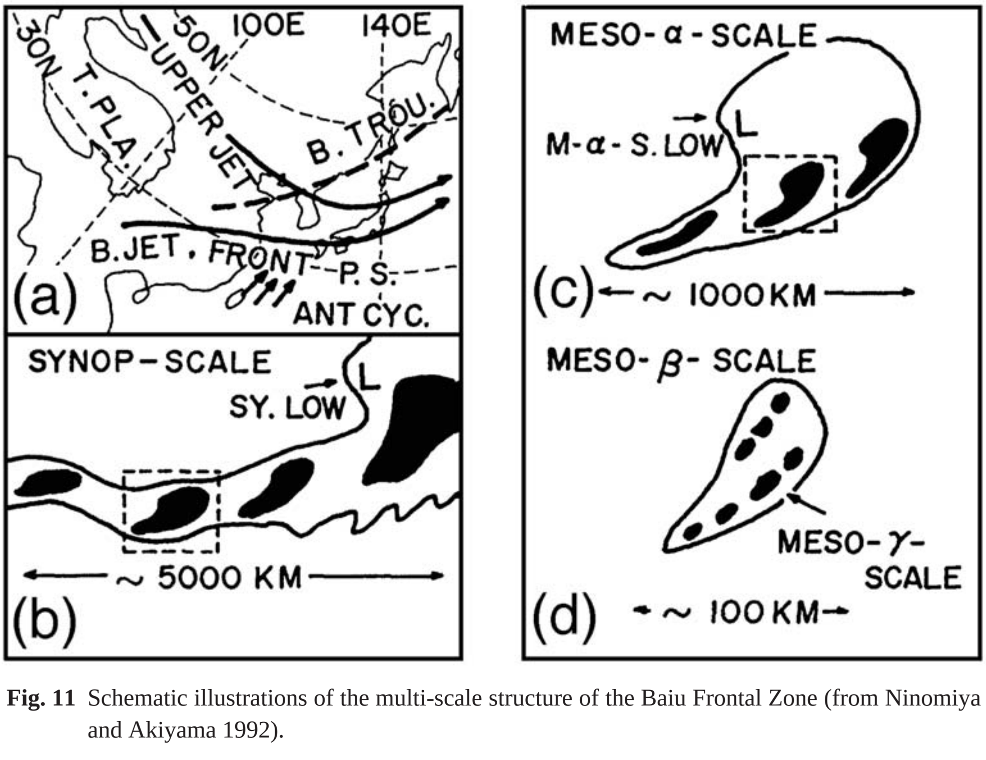

Fig. 11 Schematic illustrations of the multi-scale structure of the Baiu Frontal Zone (from Ninomiya and Akiyama 1992).

structures that occasionally give rise to torrential rainfall in confined regions (Fig. 11c). Those convective ensembles consist of meso-γ-scale convective systems (Fig. 11d). As illustrated in Fig. 11b, meso-α cyclones are often aligned along the stationary Baiu front behind a foregoing synoptic cyclone. Such a cloud pattern as illustrated in Fig. 11 is often observed during the Baiu season (from June to mid-July), as seen in the Geostationary Meteorological Satellite (GMS) 5 IR image shown in Fig. 12. Several spots of highly reflective cloudiness over southern China, the East China Sea and the western Pacific south of Japan correspond to such meso-α systems as in Fig. 11b trailing a synoptic low located over northern Japan.

Among the aforementioned multi-scale phenomena of the BFZ, global- and synoptic-scale phenomena have been realistically simulated in some AGCMs (e.g., [48]). However, realistic representation of meso-α-scale cyclones in global models is still challenging today because of insufficient spatial resolution. Simulating meso-β systems is even more challenging in global models and so currently possible only in regional models, some of which are nested on global models. Simulations with regional models (e.g., [49, 50]) show that a horizontal resolution of ~10 km is high enough to resolve many meso-β-scale features. However, the hydrostatic assumption and a particular cumulus convective parameterization scheme used in AFES should more or less distort the evolution and structure of meso-β systems. In the present study, therefore, our primary focus is upon the simulation of realistic meso-α cyclones migrating along the BFZ embedded in the Asian monsoon system.

4.2.1. MONSOON- TO SYNOPTIC-SCALE FLOWS

Fig. 13 shows the 850-hPa horizontal wind and precipitation in the Asian monsoon region simulated in AFES with T1279L96 resolution at 1800 UTC on June 26 (Day 6 of the model integration). Though somewhat overestimated, the Somali jet and monsoon westerlies downstream are well reproduced in the model. Part of that airstream reaches the northernmost part of the Bay of Bengal, after being blocked by mountains along the west coast of the Indochina peninsula. The rest appears to pass over the Indochina peninsula and then the South China Sea, finally merging itself into an enhanced low-level jet (LLJ) associated with the BFZ. The intensity of the LLJ is about 10 m s^{-1}, which is in the range of observed values. Between the BFZ and a convective region over the Western Pacific warm pool, a subtropical anticyclone is simulated in a realistic manner. The cyclonic vortex near (55°N, 150°E) corresponds to the foregoing synoptic low in the hierarchical structure of the BFZ (Figs. 11 and 12).

Overall, the precipitation pattern simulated in AFES seems quite similar to what is typically observed. For

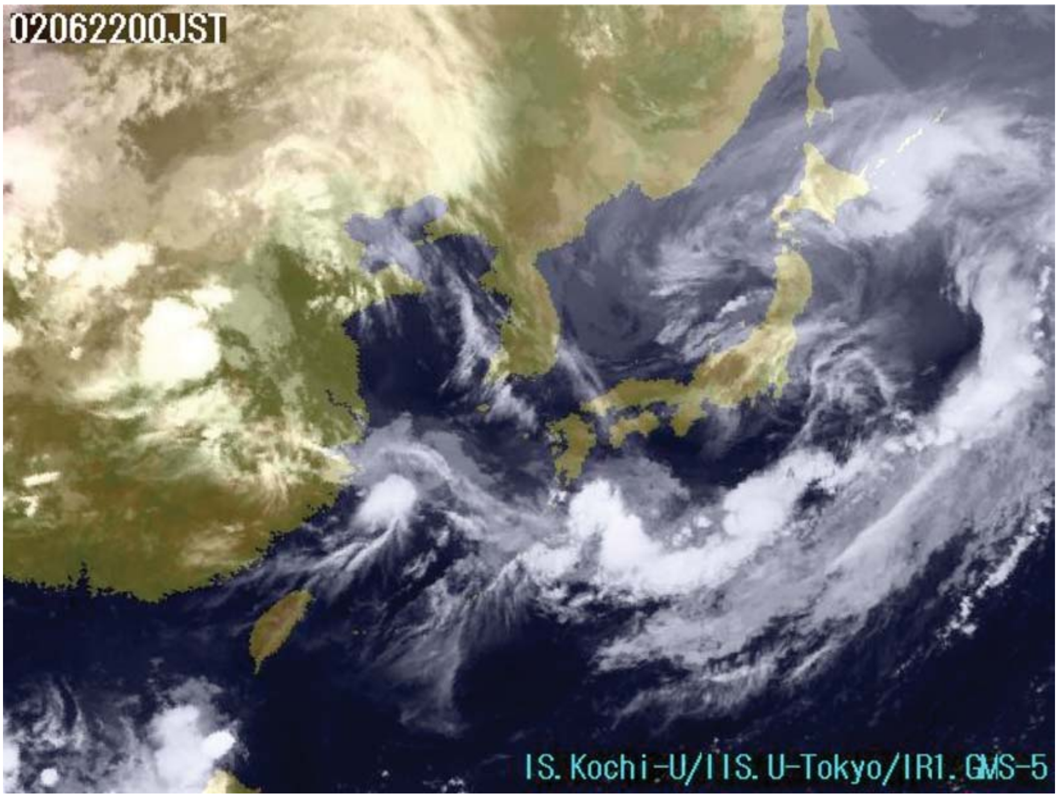

Fig. 12 GMS infrared image at 0000 UTC on 22 June 2002 (a JMA image archived at Kochi University.)

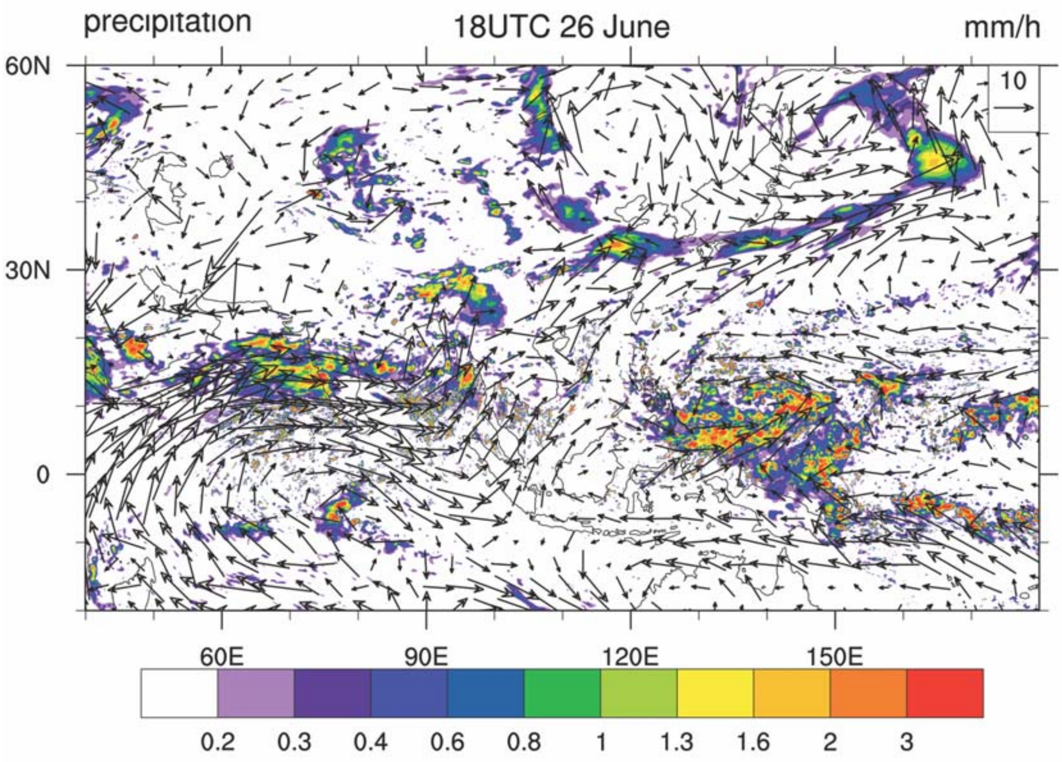

Fig. 13 Distribution of 850-hPa winds (m s^{-1}) and precipitation (mm h^{-1}) over the Asian monsoon region at 1800 UTC 26 June (Day 6) in the T1279L96 simulation

example, in addition to the intense precipitation near the synoptic low center, a zonally elongated band of enhanced precipitation formed along the BFZ with particularly heavy precipitation associated with meso-α-scale depressions. Almost all the precipitation along the BFZ is found to arise from grid condensation (not shown). However, there are a few unrealistic features in the simulation, including underestimated precipitation over the maritime continent and the South China Sea. Furthermore, rainfall appears to be overestimated over the Red and Arabian Seas and along the west coast of India, presumably due to enhanced evaporation from the sea surface and low-level convergence associated with the overemphasized Somali jet. These defects are considered as a model bias and they appear in our model simulations regardless of the horizontal resolution employed.

4.2.2. MESO-SCALE FEATURES

Fig. 14 depicts the eastward migration of a meso-α cyclone off the southern coast of Japan in a 3-hourly sequence of precipitation snapshots from 0900 to 1800 UTC on June 26 (Day 6). The phase speed of the cyclone appears to be slightly faster than that commonly observed. The phase speed estimated from a Hovmöller diagram (not shown) is about 14 m s^{-1}, which is comparable to the westerly wind speed at the 700-hPa level. Therefore the fast eastward phase migration may be attributed to the enhanced LLJ (Fig. 13). As the meso-α cyclone intensifies, a small spot (100–150 km in diameter) of particularly heavy rainfall also moves eastward together with the entire meso-α precipitation system. The rainfall rate also increases in time as the cyclone intensifies. Though somewhat weaker, precipitation also increases within several smaller spots located along the BFZ downstream of the meso-α system.

These features appear to indicate that an ensemble of meso-β systems may be simulated in our T1279L96 model as an internal structure of the meso-α precipitation complex along the BFZ, as in Fig. 11c. Unlike in cloud-resolving models, however, our simulation with the hydrostatic assumption lacks the realistic formation mechanism of individual convective systems on meso-γ or smaller scales and their ensembles. Such meso-β phenomena as back-building type quasi-stationary cloud bands are therefore unlikely to be resolved in our model, and the meso-β systems in our simulations must therefore be interpreted with caution.

Nevertheless, our model is capable of resolving fine structures in PV and θ_e fields, which may lead to the organization of meso-β-scale systems as seen in Fig. 13. For example, our T319L24 simulation produces a sharp θ_e contrast across the BFZ (Fig. 15a), and the contrast is even sharper in the T1279L96 simulation (Fig. 15b). Resolving such a “discontinuity” is impossible without a

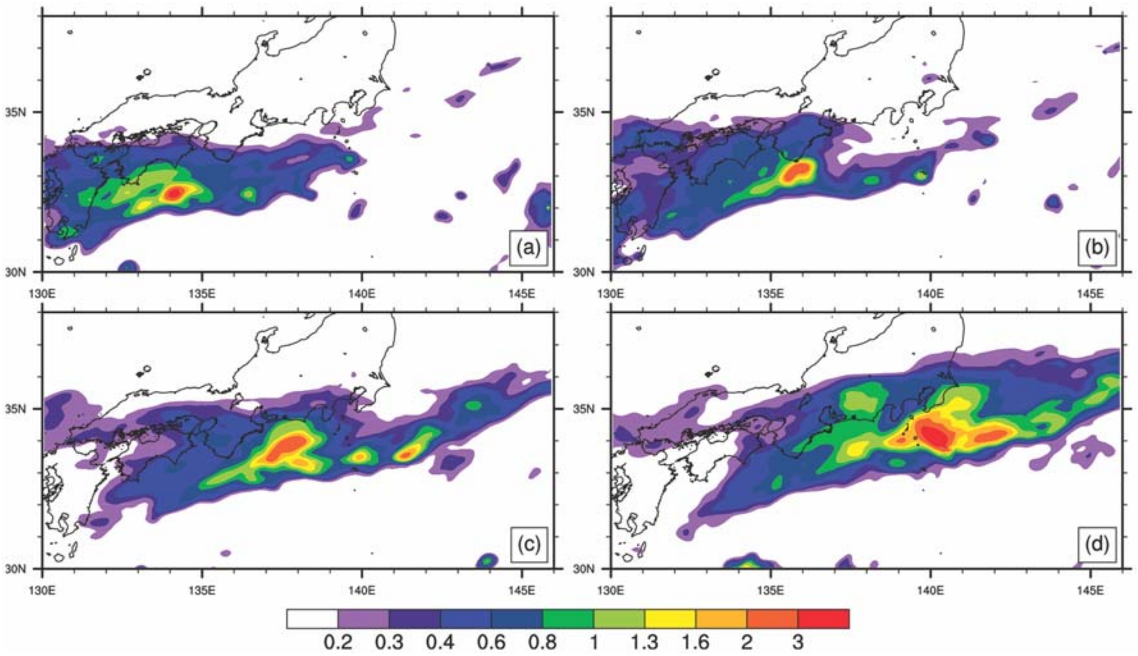

Fig. 14 Time evolution of precipitation (mm h^{-1}) in the T1279L96 simulation at 0900, 1200, 1500 and 1800 UTC on 26 June (Day 6) near Japan.

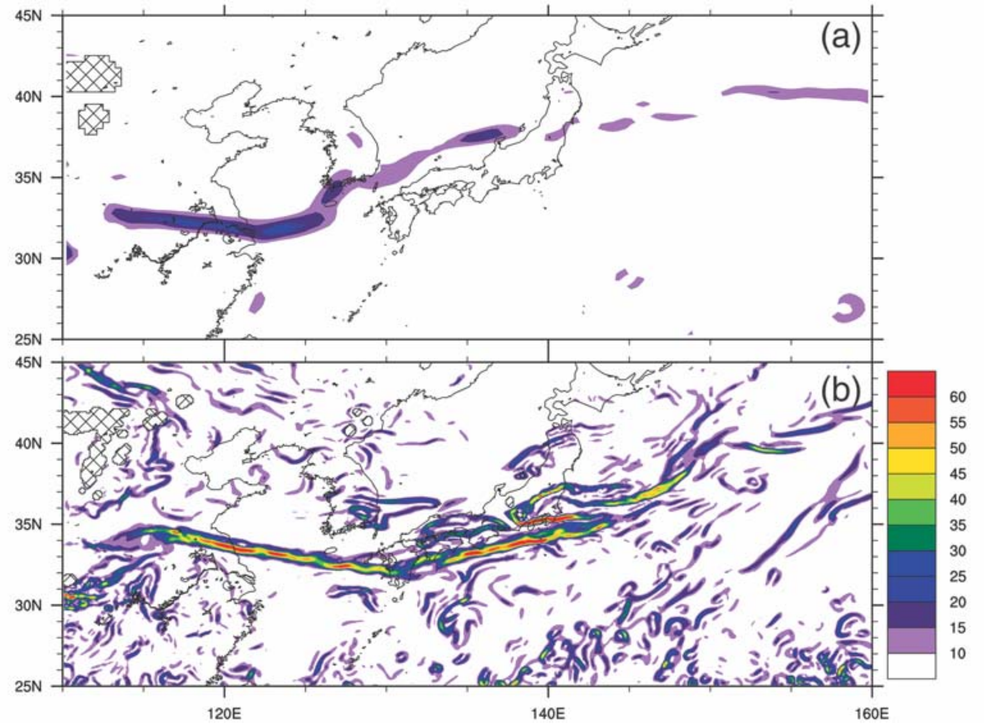

Fig. 15 Distribution of equivalent potential temperature gradient $|\Delta\theta_e|$ (K 100^{-1} km) in (a)T319L24 and (b)T1279L96 simulations on the 850-hPa level at 1800 UTC on 26 June (day 6).

very-high horizontal resolution [51]. The extremely tight PV gradient across the BFZ in the T1279L96 simulation (not shown) may act as a source of mesoscale disturbances that develop along the BFZ through the instabilities of the LLJ.

In addition, as we will demonstrate below, our model is capable of reproducing convectively unstable regions with spatial scales of 100 km or less that are formed along the BFZ under the influence of the regional topography. The resultant instability appears to be consumed by grid condensation and, to a much lesser extent, by parameterized convections along the BFZ. Thus the detailed structure of meso-α-scale disturbances is considered to be represented in a consistent manner within the dynamical framework used in the model, although the simulated meso-β-scale features and their generation mechanism may not totally be realistic.

Here, we examine the amplification of the meso-α cyclone within an unstable region generated by the topographic effect shown in Fig. 16. From a macroscopic view, θ_e gradient is tight along the BFZ (Figs. 16a and b), in a manner consistent with the observed characteristics [52]. A belt of the negative θ_e difference extends along the BFZ reflects the sloping frontal surface (Fig. 16c). In addition, there are filamentary θ_e structures along the BFZ at the 950-hPa level (Fig. 16b) in the lee of mountains

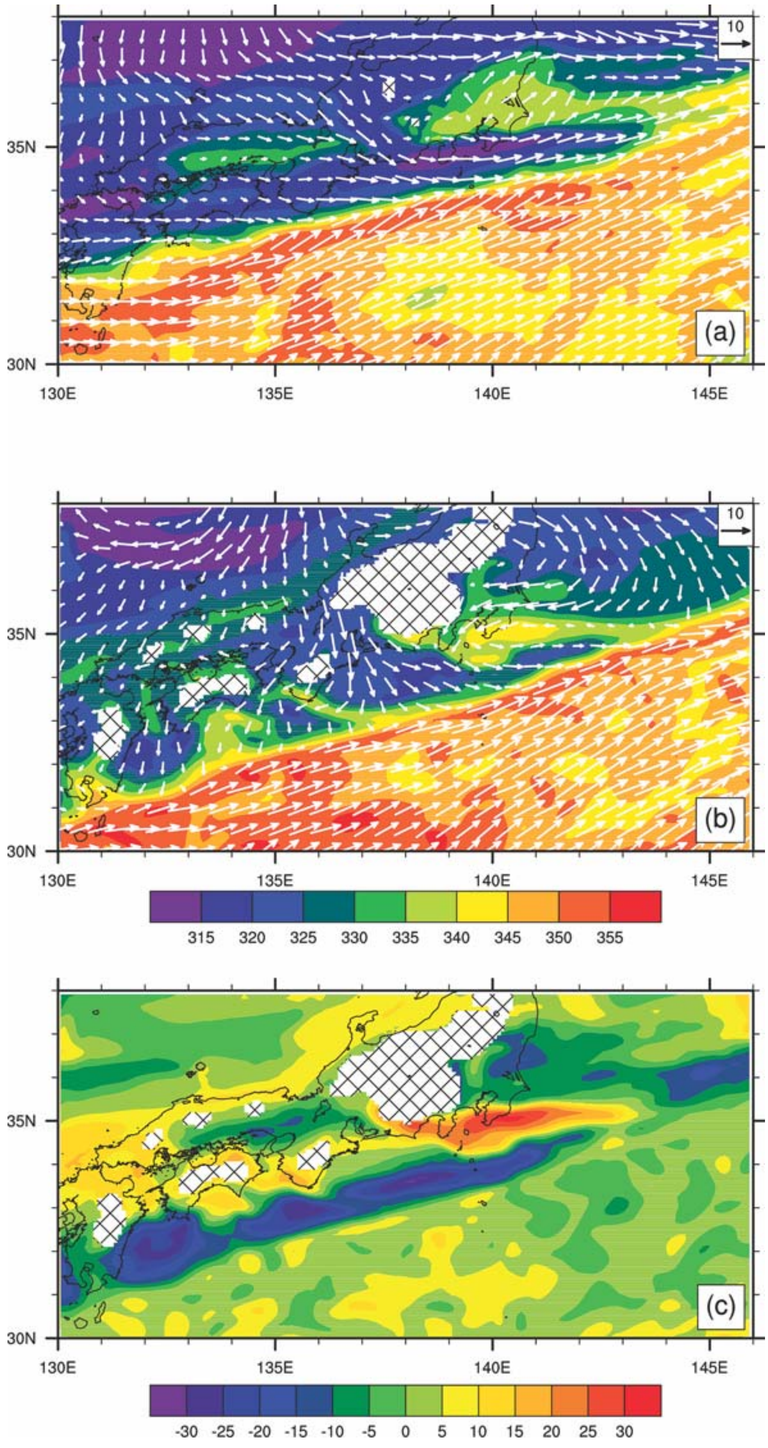

Fig. 16 Distributions of winds (m s^{-1}) and equivalent potential temperature θ_e (K) in the T1279L96 simulation on (a) 850-hPa (b) 950-hPa levels, and (c) the θ_e difference (K) between the two levels (i.e., (b) – (a)) at 1800 UTC on 26 June (Day 6) around Japan. Hatched regions represent mountains at the respective levels.

near the southern coast of Japan. As the front moves southeastward, cool and dry air intrudes through between the mountain ranges with ~1 km height, reaching the southern coast along the BFZ. Meanwhile warm and moist air is left behind on the lee side of the mountains. Thus, the filament-like structure in the near-surface moisture field is generated behind the meso-α cyclone system due to the above orographic effect of the regional terrain with horizontal scales of 50–200 km. At the 850-hPa level (Fig. 16a), in contrast, dry, cool air behind the cyclone spreads much more uniformly in the poleward side of the BFZ, blocked to a much lesser degree by those regional mountain ranges. As observed by Ninomiya and Yamazaki [53], the aforementioned vertical differential advection leads to the formation of an unstable region simulated on the lee of each of the regional terrains as shown in Fig. 16c. Among them, the region that forms downstream of the mountain range over central Japan is the largest in its extent and most unstable. Interestingly, the rapid development of the enhanced precipitation associated with the meso-α cyclone from 1500 to 1800 UTC on 26 June (Figs. 13c and d) occurs coincidentally with the formation of the convectively unstable region around that cyclone (Fig. 16c). The distinct downward increase in θ_e is confined below the 850-hPa level, indicating the confinement of convective instability within the planetary boundary layer. It is suggested that this shallow instability contributed to the development of the shallow meso-α cyclone system.

4.3. Typhoon genesis

In the AFES simulations, several tropical cyclones were formed, intensified and then moved onto the Asian continent or migrated to Japan to become extratropical cyclones. Tropical cyclogenesis may be a result of an autonomous process, which cannot be scrutinized completely in AFES because of its resolution and the dynamical constraint under the hydrostatic approximation. Yet, as observed at operational centers, there are particular large-scale configurations of the background flow that favor the formation of a tropical cyclone over a given region. AFES simulations with T1279L96 resolution are particularly suited for studying the relation of this type between the cyclogenesis and ambient flow. AFES has limitations in terms of the hydrostatic approximation and convective parameterization adopted. Nevertheless, the global coverage of AFES and its ability to simulate both the large-scale and mesoscale systems in a fairly realistic and mutually consistent manner are advantage not available to nested regional models (e.g., [54, 55]) or over global simulations with coarser resolution (e.g., [5]; see also Nagata et al. [56]). In the present report, we examine the structure and behavior of a particular typhoon simulated in an AFES T1279L96 simulation from its formation to decay stages. As described below, we obtained promising results that demonstrate the capability of AFES in simulating typhoons in the western North Pacific in summer.

4.3.1. DESCRIPTIONS OF FOUR TYPHOONS SIMULATED IN AFES

For a given instance during the model integration, the center of a typhoon, including its tropical depression stage, was detected at a particular gridpoint at which sea-level pressure (SLP) was below 1004 hPa and lower than at any of the 48 nearby gridpoints. In the T1279 model, for example, those points are confined approximately in a 70 km × 70 km horizontal domain. During the 16-day period for the T1279L96 simulation, three tropical depressions were thus identified over the northwestern Pacific (Equator–30°N, 110°E–180°) in the corresponding T319L24 integration, and two of them became strong enough to be called “typhoons”. In this study, only surface pressure gradient is used for defining “typhoons”. With the cyclostrophic relation, 2 hPa difference in about 300 km is corresponding to 12–13 m s^{-1} wind speed that is expected with a typhoon in the reality. In the T1279 integration, four “typhoons” whose tracks are shown in Fig. 17a, were identified during the same period. For our convenience, those four typhoons in the T1279 run, as well as their counterparts in the lower resolution run, will hereafter be referred to as T1, T2, T3 and T4 in the order of time of their first detection. In this sub-section we mainly focus on the evolution and structure of T3, the most intense typhoon found in our integration period. Surprisingly, no corresponding storm was generated in the T319 integration.

Before discussing T3 in detail, it may be informative to briefly describe the tracks of the three other typhoons in a pair of the AFES integrations with different resolutions. The typhoon T1 was already present in the initial condition. During the period of September 6–10, T1 in the T1279 run intensifies near Okinawa Island and then moves northward in the East China Sea before passing through the Tsushima Straight. It finally makes landfall on the Noto Peninsula at the Japan Sea side of Honshu Island of Japan. The corresponding typhoon in the T319 integration develops in the East China Sea as it moves northward before making landfall on the Korean Peninsula. In each of the simulations T1 finally becomes an extratropical cyclone. The typhoon T2 in the T1279 simulation appears on September 10 far south of Japan. It moves westward into the South China Sea and then decays upon reaching Hainan Island. In contrast, T2 in the T319 integration gradually develops over the northwestern Pacific as it moves westward then turns toward the north, before weakening into an extratropical cyclone

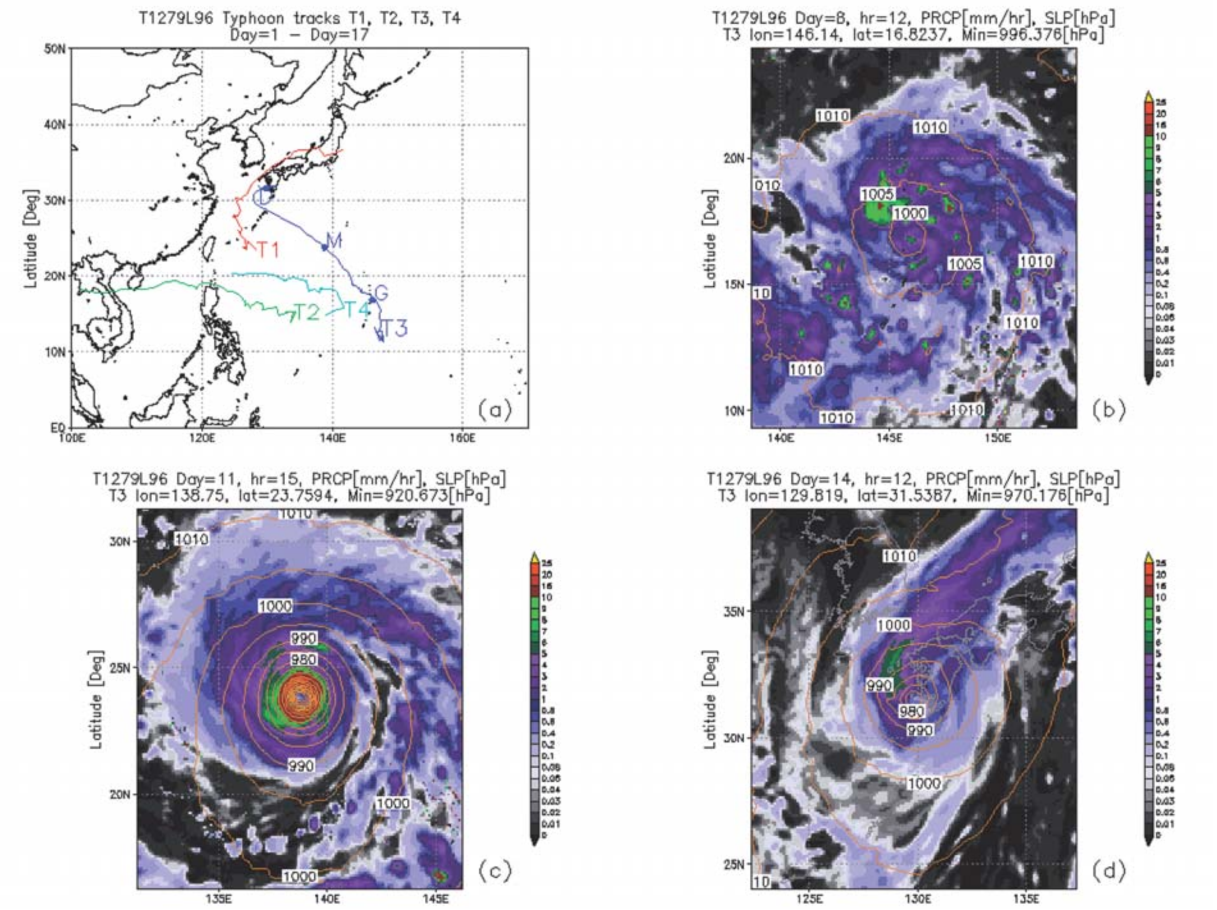

Fig. 17 (a) Typhoon tracks detected in the T1279 AFES simulation during the integration period of 16 days. (b) Snapshot distributions of precipitation intensity (PRCP) and SLP around the typhoon T3 center at the formation stage when the center is at 16.82°N and 146.14°E with the minimum pressure of 996.4 hPa, (c) for the mature stage at 23.76°N and 138.75°E, 920.7 hPa, and (d) for the decay stage at 31.54°N and 129.82°E, 970.2 hPa. The contour interval for SLP is 5 hPa except for near the center area in (d). The domain of each panel is 15 degrees in longitude and latitude.

over Kyushu Island of Japan. The typhoon T4 is simulated as a westward moving tropical depression over the last two days of the T1279 integration.

Time change of the minimum surface pressure is shown in Fig. 18 for each of the four typhoons mentioned above. The intense typhoon T3 deepened at about the same rate as T2 and Rapidly weakened after mature stage. The plots in the figure reveal semidiurnal variation in the surface pressure. Such an oscillation exists over the ocean arean in AFES, with its amplitude decreasing from a little more than 1hPa at 10°N to its half at 30°N. Hunt and Manabe [57] made a detailed investigation on the similar feature simulated in their model. Based on their analysis, we assume that the semidiurnal pressure variation noted in AFES is real and is excited by absorption of solar radiation by water vapor.

4.3.2. THREE STAGES OF TYPHOON T3

Here we look at the distributions of surface pressure and precipitation intensity for the Typhoon T3 in the T1279 run at three different stages of its life cycle. It forms around September 13, a week after the initiation of the integration. Snapshots at 8 days and 12 hours after the start of the integration are chosen from the formation, mature and decay stages, respectively. Distributions of SLP and precipitation intensity (PRCP) in a domain spanning 15° both in longitude and latitude and based at the storm center are shown in Figs. 17b, 17c and 17d for the three respective stages. The minimum SLP values at the storm center for the respective stages are 996.4, 920.7 (the lowest in the entire life cycle), and 970.2 hPa.

As illustrated in Fig. 17a, T3 forms in the western North Pacific to the east of T2. It is evident in Fig. 17b that concentric isobars and spiral PRCP bands are already present. During next three days T3 develops into a very strong typhoon. Both SLP and PRCP clearly suggest the formation of a "typhoon eye", that is recognized as a compact non-precipitating area at the storm center, surrounded by a heavily precipitating "eyewall" (Fig. 17c). Outside of this storm core region, PRCP is organized into spiral bands with ~50 km in width, exhibiting marked similarities with typhoon cloud bands typically observed

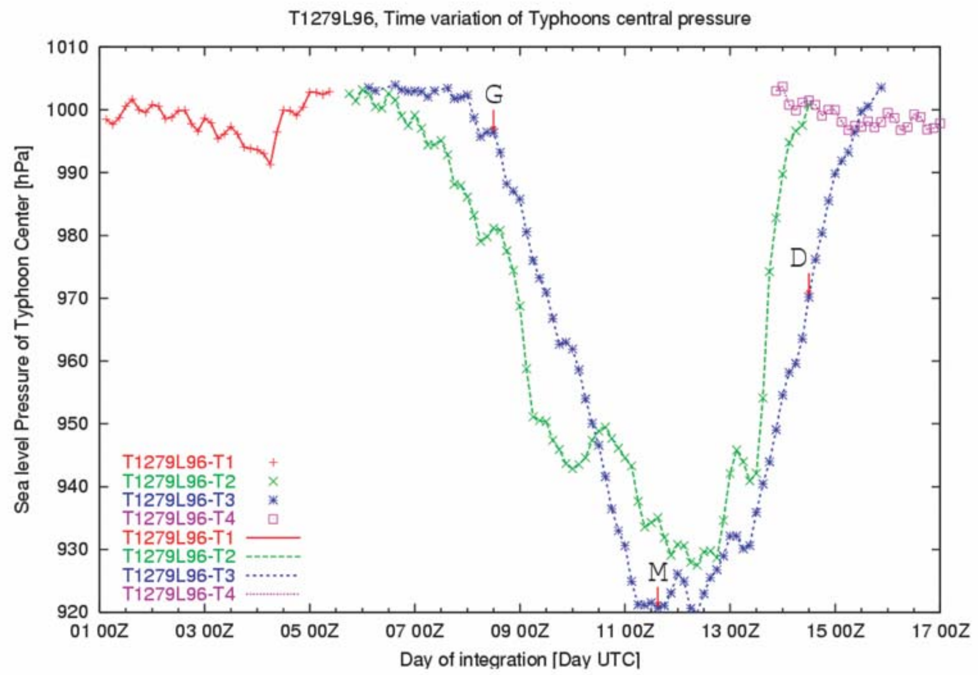

Fig. 18 Time series of the sea level pressure at the center of typhoons, T1, T2, T3 and T4 during 16 days. Red solid line marked with plus is for T1's, green long break line marked with cross is for T2's, blue short break line marked with double asterisk is for T3's and pink dot line marked with open square is for T4's. All of typhoons central pressure data marked on the figure are sampled every three hours. "G", "M" and "D" point T3's major 3-stages, which mean "generating", "mature" and "decay" corresponding to fig.17 (b), (c) and (d), respectively.

in satellite images. Though it weakens gradually in moving northward, T3 makes landfall on the Kyushu Island of Japan, as a powerful typhoon of 980 hPa. Fig. 17d presents a snapshot just before landfall. Within a day after landfall, T3 becomes an extratropical cyclone moving across the Honshu Island of Japan. By this transition stage, its structure typical for a tropical storm in which an axially symmetric SLP pattern has been distorted with the disappearance of the typhoon eye and eyewall. Only a remnant of the spiral PRCP bands is noticeable in Fig. 17d. Unlike at the formation and mature stages, no spots of intense rainfall are evident in and around the PRCP bands in the outer region of the storm. Rather, PRCP is heavy along a band extending northeastward from the western part of the storm core toward a persistent midlatitude surface front, which is associated with an upper-level trough approaching from the west.

4.3.3. TIME EVOLUTION OF VERTICAL STRUCTURE OF T3

The time evolution in the T3 structure is depicted in Figs. 19, 20 and 21, which show vertical cross sections over 15° longitudinal spans through the T3 center for the three different stages corresponding to Figs. 17b, 17c and 17d, respectively. Panels in each of the figures are based on snapshots of (a) θ_e, (b) specific humidity (contoured) and temperature deviations at each σ level from their longitudinal means, (c) wind vector (arrows, consisting of vertical and zonal velocities) and zonal wind (contoured), and (d) temperature (contoured) and meridional (i.e., tangential) wind velocity. The sequence of the Panels (a), (b) and contours in (d) in the three figures reveals the evolution of the thermodynamic state of T3, whereas that of panels (c) and (d) indicates the evolution of its dynamical condition.

The thermodynamic state at the formation stage is characterized by the warm moist planetary boundary layer (PBL) below the storm and also by numerous small-scale weak warming and moistening areas scattered within a fairly broad longitudinal span in the free troposphere (Figs. 19a and 19b). The position of the deepest moistening coincides with heavy PRCP occurring at 148°E along the innermost spiral rain band to the east of the storm center. A shallower spot of relatively warm and moist air at 151°E corresponds to another spiral band farther away from the center. A hint of an upper-tropospheric warm core appears right above the storm center (Fig. 19b). The wind field shows interesting features. The zonal wind distribution suggests that T3 develops in an area where the PBL air converges because of particularly strong easterlies to the east of the storm center. In the free atmosphere, the convergence is associated with the westerlies in a region west of the storm. At the tropopause level the flow is

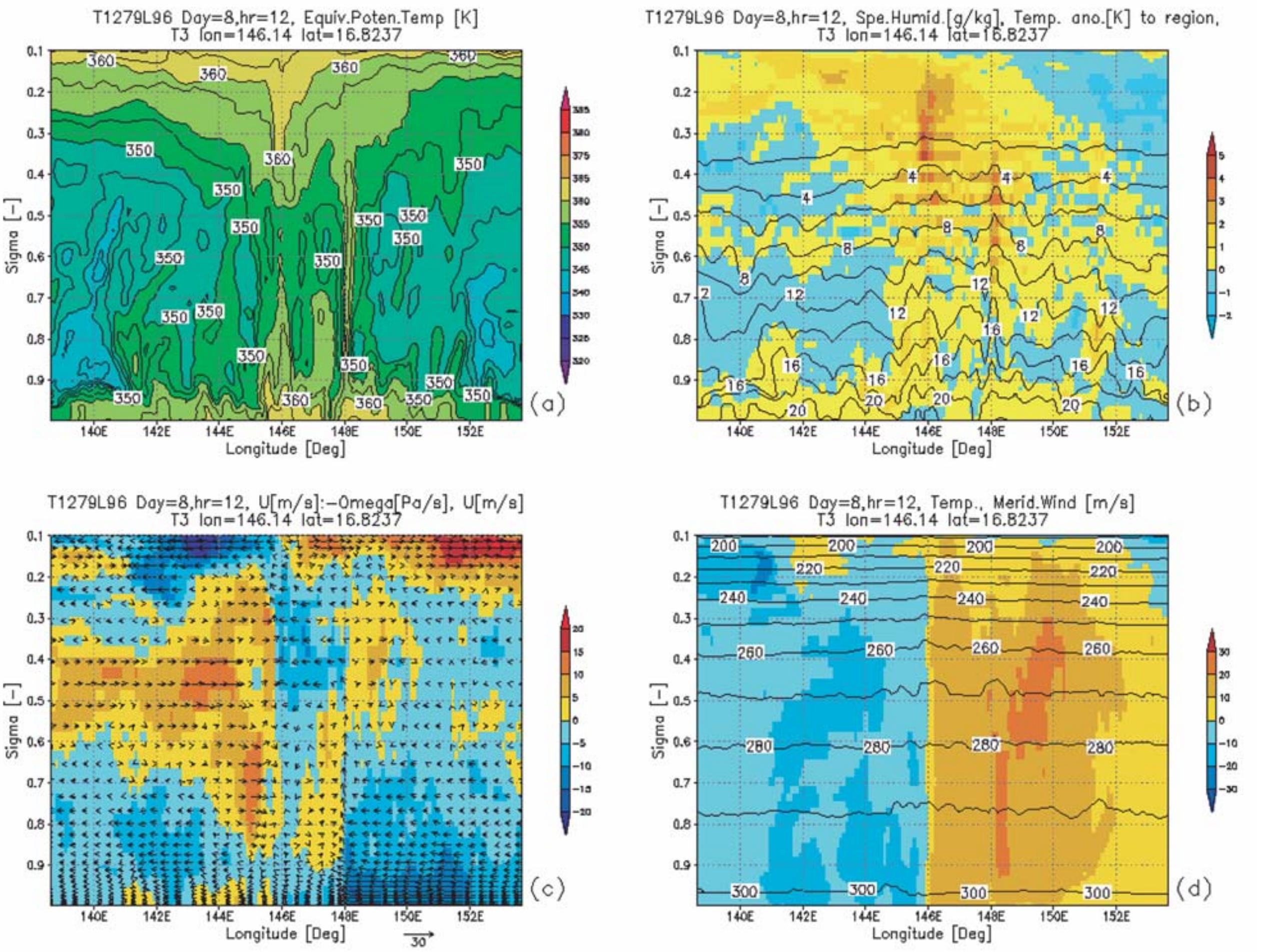

Fig. 19 Snapshot longitude-height sections across the storm center of T3 at the formation stage corresponding to Fig. 17b: (a) Equivalent potential temperature (K); (b) Temperature deviation (K) from the sigma level average for the longitudinal extent (shade), with specific humidity (g kg^{-1}) distribution (contours); (c) vectors of the zonal and vertical wind components (unit: m s^{-1} and Pa s^{-1}, respectively, plotted at 4-grids intervals) superimposed on the distribution of zonal wind (m s^{-1}; westerlies positive); and (d) temperature (contours with 10 K contour interval) and the distribution of meridional wind (shade: southerlies positive).

diverging out above the weak warm core. The meridional wind field indicates that the storm already takes a form of well-defined cyclonic vortex, which is consistent with the SLP pattern in Fig. 17b. The southerly wind component exhibits a maximum just outside of the innermost spiral rain band located ~300 km away from the center. There the surface wind speed reaches up to 15 m s^{-1}.

By the mature stage, the thermodynamic state becomes much more coherent. The distinct core exists in which θ_e has undergone a marked increase throughout the troposphere (Fig. 20a). As apparent in Fig. 20b, the θ_e increase is due to both warming and moistening. Signatures of rainbands are detectable at this stage. Conditional instability almost disappears in the eyewall, which exhibits an outward tilt with height (Figs. 20b and d). This implies that the eyewall portion of the storm simply represents mesoscale circulation. In the mid- and upper troposphere, the typhoon eye is less humid and considerably warmer than in the eyewall. In fact, sinking motion is hinted within the eye (Fig. 20c). According to Kurihara and Bender [58], the vertical motion in the eye has a large transient component that tends to mask the mean sinking motion obtainable through time averaging, say, over a 10-hour period. At the lower levels in the eye, θ_e increases downward, indicative of a conditionally unstable state. Probably the moisture is supplied into the eye from the PBL. Further study is needed to clarify the heat budget in the typhoon core. Wind vectors shown in Fig. 20c indicate a strong outflow from the warm core at the tropopause level and an inflow in the thickened PBL. They also indicate that the storm is still in the region of the easterlies. The meridional wind distribution shows that the storm core is compact with its axis standing almost straight. The tangential wind speed right around the eyewall reaches above 60 m s^{-1}.

Dramatic changes in the T3 structure occur between

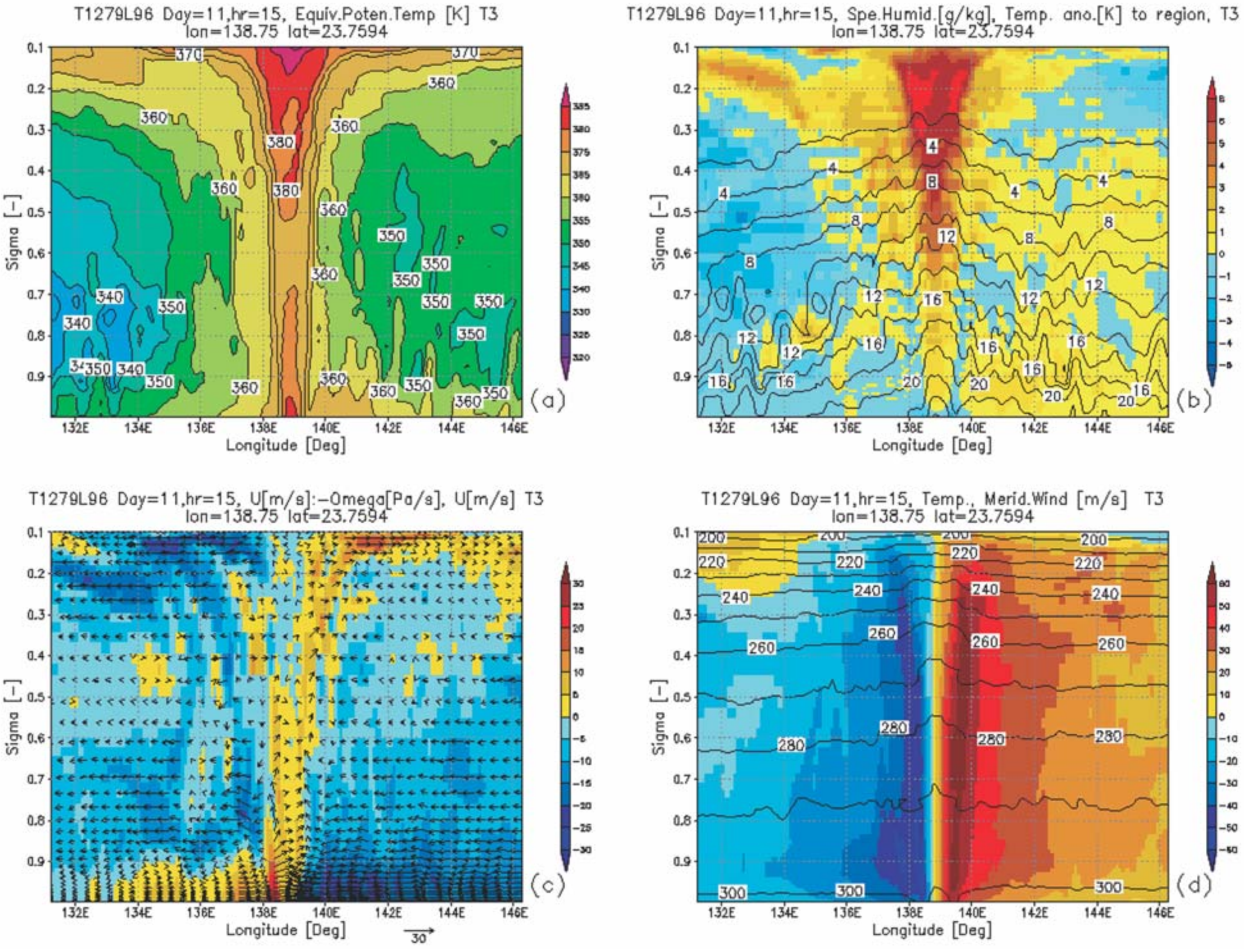

Fig. 20 Same as in Fig. 19 but for the mature stage corresponding to Fig. 16c.

the mature and decay stages. As evident in Fig. 21c, the storm is now at the latitudes where the ambient flow is generally westerly. One of the prominent changes is the vertical tilting of the storm core (Fig. 21a). In the mid-troposphere, the tilted core is still somewhat drier than its immediate surroundings but not as warm as before (Fig. 21b). Instead, the warmest air is located to the east of the tilted upper-level core right above the surface storm center. Seemingly, the strong ascending motion in the mid- and lower troposphere slightly to the west of the storm core (Fig. 21c) is connected to a midlatitude stationary front. As the vortex weakens, the storm becomes less compact as suggested by the increasing radius of the maximum tangential wind (Fig. 21d).

4.3.4. AXIAL ASYMMETRIES IN T3 STRUCTURE

Figs. 19, 20 and 21, particularly, their Panels (a) and (b), show remarkable evolution of west-east asymmetries across the storm axis. As depicted in Figs. 19a and 19b, it is generally warmer and more humid to the east of the storm center, implying relatively large potential for convective activity there. This asymmetric feature becomes clearer as T3 evolves into the mature stage and then into the transition stage at midlatitude. The degree of the axial asymmetries is quantified for each of the levels of $\sigma = 0.2$, 0.5 and 0.85 by comparing θ_e values at the western and eastern edges of the domain plotted in Panel (a) in each of the figures against θ_e at the longitude of the surface storm center (Table 2). In the upper troposphere ($\sigma = 0.2$), the axial asymmetries in θ_e are the greatest at the mature stage as a distinct warm core develops right above the storm center. The asymmetries are reduced by the decay stage, as the upper-level warm core is weakened and displaced slightly to the west of the surface storm center (Fig. 21b). At the mid-tropospheric level ($\sigma = 0.5$), the axial asymmetries, especially the θ_e deviation at the western edge, increase by the mature stage and remain strong until the decay stage. Meanwhile, the axial asymmetries at the lower levels ($\sigma = 0.85$) keep increasing throughout the life cycle of T3 especially at its western edge. Apparently, T3 undergoes distinct structural changes, losing its axial symmetry as the primary characteristic of a tropical cyclone until its transition into an extratropical system.

One of the important processes that contribute to the

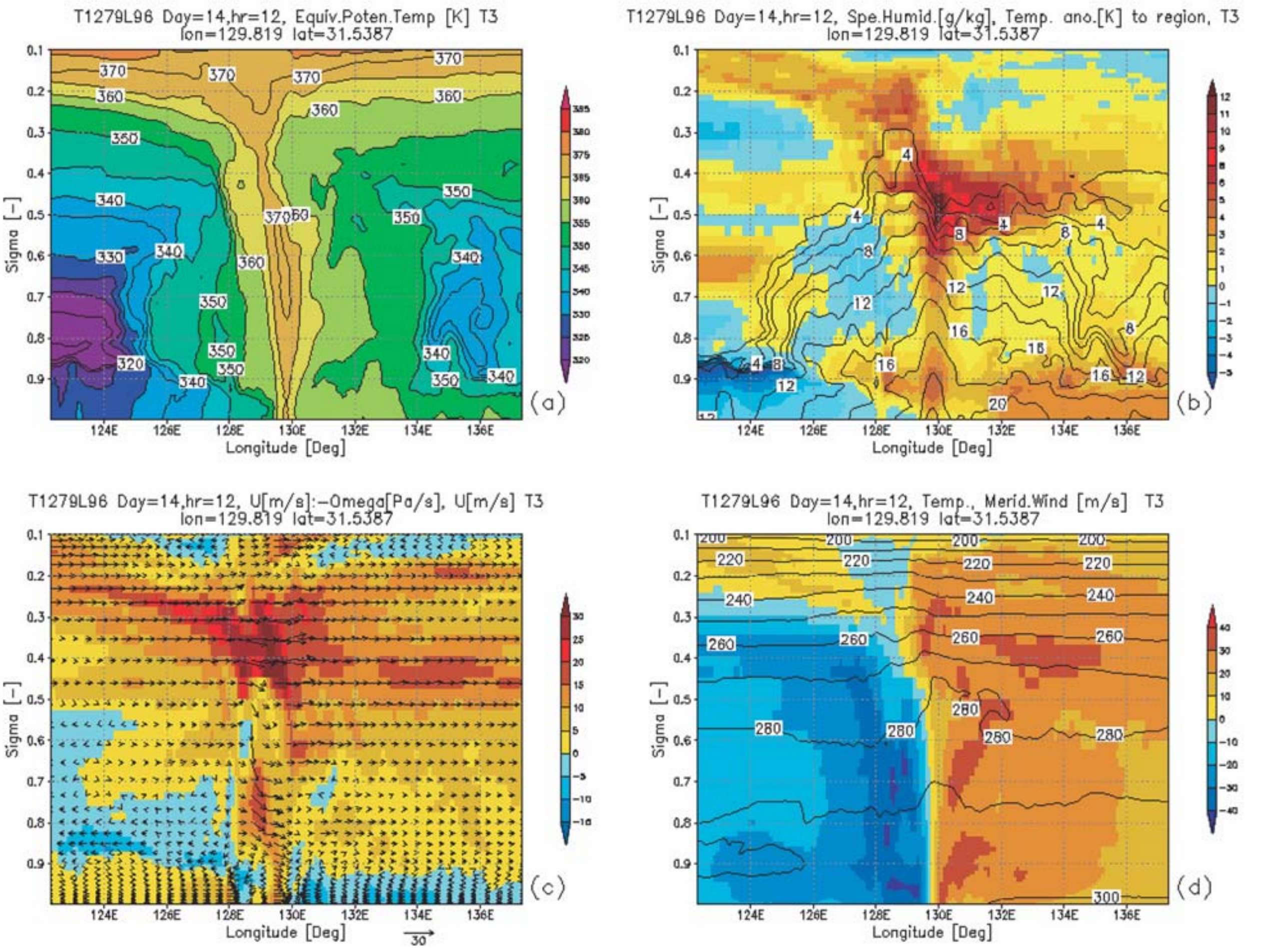

Fig. 21 Same as in Fig. 19 but for the decay stage corresponding to Fig. 16d.

Table 2 Equivalent potential temperature (K) asymmetry. Values at the center and at the western and eastern edges of the cross sections in Figs. 19a, 20a and 21a are listed for each of the levels of $\sigma = 0.2$, 0.5 and 0.85. Numbers in parenthesis are the deviation from the center value.

	Formation stage			Mature stage			Decay stage		
	west	center	east	west	center	east	west	center	east
$\sigma = 0.2$	357 (–5)	362	354 (–8)	361 (–19)	380	358 (–22)	363 (–9)	372	360 (–12)
$\sigma = 0.5$	348 (–9)	357	347 (–10)	343 (–32)	375	352 (–23)	335 (–35)	370	343 (–27)
$\sigma = 0.85$	343 (–15)	358	344 (–14)	344 (–26)	370	353 (–17)	320 (–47)	367	343 (–24)

development of the axial asymmetries of T3 is its cyclonic wind acting on the zonally inhomogeneous θ_e field related to the SST distribution, midlatitude baroclinicity and land-sea contrast, etc. We speculate that, when T3 moves up near Kyushu, relatively cold (warm) and dry (moist) air is transported to the west (east) of the storm from the north (south). The cool and very dry air (specific humidity less than 4 g kg^{-1}) to the west of T3 as seen in Fig. 21b, is probably related to the advection of a continental air mass and also influenced perhaps by an upper-level trough approaching from the west. The strong thermal contrast across the storm center, among many factors, can induce an overturning that contributes to the tilting of the storm axis.

We emphasize that our detailed description of the T3 structure, including the tilt of the storm core at the decay stage, would be impossible without the use of numerical products from a high-resolution model such as our AFES with T1279 resolution. Presumably, the ability of AFES to simulate such marked intensification as seen in the powerful typhoon T3 lies in its capability to represent a compact warm core in a typhoon "eye" and the intense convective activity along the surrounding "eyewall" in a realistic manner. Though fairly realistic in many respects, typhoons simulated in the T319 integration tend to be weaker than their counterparts in the T1279 integration, with their "eyes" being more diffuse. Of course, nested mesh models have been developed for resolving fine structures around a tropical cyclone core with a resolution as high as the T1279-version of AFES (e.g., [54]). Even those regional models, however, sometimes fail to reproduce rapid intensification of a typhoon [56]. Furthermore, their application capability is rather limited as compared to AFES. For example, a multi-storm situation cannot be easily handled in a nested model.

5. Concluding Remarks

In this article an overview is presented for a set of global simulations with AFES conducted on the ES with ultra-high resolution of T1279L96 (equivalently, 10 km horizontally and 500 m vertically in the free atmosphere with much finer resolution near the surface). To our best knowledge, it is one of the first attempts for such an ultra-high-resolution global AGCM experiment[1], which is possible at this moment only with AFES whose code has been tuned for the extreme integration efficiently on the ES [8]. One of the greatest advantages of an ultra-high resolution global integration with AFES is its ability to simulate the interaction among planetary, synoptic and meso-scale phenomena. We have presented evidence in this article that such interaction is indeed simulated in a fairly realistic manner, as in our examples of wintertime extratropical cyclogenesis in the North Pacific, a polar low over the Far East, and the Baiu (Meiu) front system and typhoon genesis over the western North Pacific. Of course, our analysis is rather preliminary and a more careful evaluation of the simulations against the observations is necessary. Yet, our analysis indicates that high-resolution AFES simulations are useful in investigating self-organization of mesoscale systems under the influence of large-scale circulations and the feedbacks from the former to the latter.

Our T1279 AFES simulations were limited to only 10–16-day long, mainly because of the overwhelming data volume of the output. Although the computational efficiency of AFES allows a seasonal integration with the T1279L96 resolution to be completed within a few weeks or so of real time, the output of such a simulation would currently be too large to handle. In fact, an instantaneous three-dimensional field of a given variable in the output of a T1279L96 simulation is as large as 2.6 GB, even if stored in single precision. If one stores ten of those variables as a 6-hourly output, a 100-day simulation would yield about 10 TB of data.

Thus far, AFES may be regarded merely as a higher-resolution version of a conventional AGCM. We have plans to "modernize" AFES[2]. For example, we are planning to adopt physical parameterizations used in regional mesoscale models. Also, we are now implementing a conservative semi-Lagrangian (CSL) scheme developed by Xiao et al. [59]. Preliminary results indicate that an introduction of the CSL scheme to the water vapor transport has yielded some significant improvement in the vapor distribution and rainfall pattern, especially over arid and mountain areas. Furthermore, we are planning to implement the CSL scheme into the entire dynamical core, which will enable increasing the time step for numerical integration. If our data storage allows, we may be able to use the ultra-high resolution AFES in future in the study of decadal or centennial-scale changes in their ensemble activity of mesoscale phenomena. For example, we may be able to see what changes would occur under the warmed climate in the intensity, frequency and tracks of tropical cyclones in more detail than in any other model simulations currently available. We may also be able to see the corresponding changes in regional heavy precipitation associated with the Asian Monsoon, Baiu-front or other tropical or midlatitide convective activity and also in the behavior of polar lows under the warmed climate. AFES will allow us to further investigate the dynamical and thermodynamical mechanisms of interaction between those modified mesoscale phenomena under the regional topographic effects and larger-scale circulation changes.

Acknowledgments

The authors would like to thank the Center for Climate System Research, the University of Tokyo, and National Institute for Environmental Studies of Japan for kindly having made their AGCM available to our project. The authors would like to express our sincere gratitude to the late Prof. Atusi Numaguti, who was the central force of

---

[1] The authors have recently learnt that a group at GFDL/NOAA, Princeton, NJ, USA, performed a global 10-km mesh nonhydrostatic simulation with their model, ZETAC. See their homepage (http://www.gfdl.noaa.gov) for details.

[2] The CCSR/NIES AGCM, from which the original code of AFES was adopted, has now been upgraded to include more sophisticated parameterizations of physical, chemical and biological processes in the atmosphere and around its lower boundary.

developing the CCSR/NIES model. This paper is dedicated to the late Mr. Miyoshi, since we all recognize that the Earth Simulator could never been realized without his ambitious enthusiasm for next-generation supercomputing. The authors also would like to thank Dr. Tetsuya Sato, NEC, Japan Agency for Marine-Earth Science and Technology, The OFES and CFES Teams, and Frontier's Climate Variations Research Program (director: Prof. Toshio Yamagata) for their enthusiastic support. The development of AFES was impossible without hard work by Messrs. Satoru Shingu, Hiromitsu Fuchigami and Masayuki Yamada. Prof. Kevin P. Hamilton's and Prof. Julia Slingo's comments on the manuscript of this paper improved the readability very much.

(This article is reviewed by Dr. Julia Slingo.)

References

[1] A. J. Simmons, and A. Hollingsworth, Some aspects of the improvement in skill of numerical weather prediction, *Quart. J. Roy. Meteor. Soc*., vol.128, pp.647–677, 2002.

[2] K. Hamilton, R. J. Wilson, J. D. Mahlman, and L. J. Umscheid, Climatology of the SKYHI Troposphere-Stratosphere-Mesosphere General Circulation Model, *J. Atmos. Sci*., vol.52, pp.5–43, 1995.

[3] K. Hamilton, R. J. Wilson, and R. H. Hemler, Middle Atmosphere Simulated with High Vertical and Horizontal Resolution Versions of a GCM: Improvement in the Cold Pole Bias and Generation of a QBO-Like Oscillation in the Tropics, *J. Atmos. Sci*., vol.56, pp.3829–3846, 1999.

[4] K. Hamilton, R. J. Wilson, and R. H. Hemler, Spontaneous Stratospheric QBO-Like Oscillations Simulated by the GFDL SKYHI General Circulation Model, *J. Atmos. Sci*., vol.58, pp.3271–3292, 2001.

[5] K. Hamilton, and R. S. Hemler, Appearance of a supertyphoon in a global climate model simulation, *Bull. Amer. Meteor. Soc*., vol.78, pp.2874–2876, 1997.

[6] A. L. Conaty, J. C. Jusem, L. Takacs, D. Keyser, and R. Atlas, The structure and evolution of extratropical cyclones, fronts, jet streams, and the tropopause in the GEOS General Circulation Model, *Bull. Amer. Meteor. Soc*., vol.82, pp.1853–1867, 2001.

[7] T. Sato, S. Kitawaki, and M. Yokokawa, Earth Simulator running, *Int Supercomputing Conf*, June 2002.

[8] S. Shingu, H. Takahara, H. Fuchigami, M. Yamada, Y. Tsuda, W. Ohfuchi, Y. Sasaki, K. Kobayashi, T. Hagiwara, S. Habata, M. Yokokawa, H. Itoh, and K. Otsuka, A 26.58 Tflops Global Atmospheric Simulation with the Spectral Transform Method on the Earth Simulator, *Proceedings of the ACE/IEEE SC2002 conference,* 2002. http://www.sc-2002.org/paperpdfs/pap.pap331.pdf .

[9] I. Orlanski, and J. Katzfey, The life cycle of a cyclone wave in the Southern Hemisphere. Part I: Eddy kinetic energy budget, *J. Atmos. Sci*., vol.48, pp.1972–1998, 1991.

[10] E. K. M. Chang, Characteristics of wave packets in the upper troposphere. Part II: Seasonal and hemispheric variations, *J. Atmos. Sci*., vol.56, pp.1729–1747, 1999.

[11] U. Cubasch, G. A. Meehl, G. J. Boer, R. J. Stouffer, M. Dix, A. Noda, C. A. Senior, S. Raper, and K. S. Yap, Projections of future climate in *Climate Change 2001: The Scientific Basis. Contribution of Working Group I to the Third Assessment Report of the Intergovernmental Panel on Climate Change*, *Houghton*, J. T., Y. Ding, D. J. Griggs, M. Noguer, P. J. van der Linden, X. Dai, K. Maskell and C. A. Johnson, Eds., Cambridge University Press, pp.525–582, 2001.

[12] W. L. Gates, J. Boyle, C. Covey, C. Dease, C. Doutriaux, R. Drach, M. Fiorino, P. Gleckler, J. Hnilo, S. Marlais, T. Phillips, G. Potter, B. Santer, K. Sperber, K. Taylor, and D. Williams, An Overview of the Results of the Atmospheric Model Intercomparison Project (AMIP I), *Bull. Amer. Meteor. Soc*., vol.73, pp.1962–1970, 1998.

[13] T. N. Krishnamurti, H. S. Bedi, and V. M. Hardiker, *An Introduction to Global Spectral Modeling*, Oxford University Press, Oxford, United Kingdom, 1998.

[14] S. A. Orszag, Transform method for calculation of vector-coupled sums: Application to the spectral form of the vorticity equation, *J. Atmos. Sci*., vol.27, pp.890–895, 1970.

[15] N. A. Phillips, A coordinate system having some special advantages for numerical forecasting, *J. Meteor*., vol.14, pp.184–185, 1957.

[16] A. Numaguti, S. Sugata, M. Takahashi, T. Nakajima, and A. Sumi, Study on the climate system and mass transport by a climate model, *CGER's Supercomputer Monograph*, vol.3, Center for Global Environmental Research, National Institute for Environmental Studies, Tsukuba, Japan, 1997.

[17] T. Nakajima, and M. Tanaka, Matrix formulation for the transfer of solar radiation in a plane-parallel scattering atmosphere, *J. Quant. Spectrosc. Rdiat. Transfer*, vol.35, pp.13–21, 1986.

[18] A. Arakawa, and W. H. Schubert, Interactions of cumulus cloud ensemble with the large-scale environment. Part I, *J. Atmos. Sci*., vol.31, pp.671–701, 1974.

[19] G. L. Mellor, and T. Yamada, A hierarchy of turbulence closure models for planetary boundary layers, *J. Atmos. Sci*., vol.31, pp.1791–1806, 1974.

[20] S. Yamane, M. Honda, H. Nakamura, and W. Ohfuchi, On interdecadal modulations of prominent variability of boreal winter general circulation field on the Northern Hemisphere appearing in both observational data and numerical simulations -With special attention to the seesaws between the Aleutian and Icelandic lows, *Gross Wetter*, vol.40, pp.88–97 (in Japanese), 2002.

[21] M. Yamasaki, A three-dimensional tropical cyclone model

with parameterized cumulus convection, *Papers Meteor. Geophys*., vol.37, pp.205–234, 1986.

[22] M. Yamasaki, A tropical cyclone model resolving mesoscale organized convection with prognostic treatment of subgrid-scale cloud water, *J. Meteor. Soc. Japan*, vol.79, pp.637–655, 2001.

[23] E. Kalnay, M. Kanamitsu, R. Kistler, W. Collins, D. Deaven, L. Gandin, M. Iredell, S. Saha, G. White, J. Woolen, Y. Zhu, M. Chelliah, W. Ebisuzaki, W. Higgins, J. Janowiak, K. C. Mo, C. Roplewski, J. Wang, A. Leetmaa, R. Reynolds, R. Jenne, and D. Joseph, The NCEP/NCAR 40-year reanalysis project, *Bull. Amer. Meteor. Soc*., vol.77, pp.437–471, 1996.

[24] N. A. Rayner, D. E. Parker, E. B. Horton, C. K. Folland, L. C. Alexander, D. P. Rowell, E. C. Kent, and A. Kaplan, Global analyses of SST, sea ice and night marine air temperature since the late nineteenth century, *J. Geophys. Res*., 2003 (to be submitted).

[25] R. Gall, A comparison of linear baroclinic instability theory with the eddy statistics of a general circulation model, *J. Atmos. Sci*., vol.33, pp.349–373, 1976.

[26] A. J. Simmons, and B. J. Hoskins, Baroclinic instability on the sphere: Solutions with a more realistic tropopause, *J. Atmos. Sci*., vol.34, pp.581–588, 1977.

[27] M. Christoph, U. Ulbrich, and P. Speth, Midwinter suppression of Northern Hemisphere storm track activity in the real atmosphere and in GCM experiments, *J. Atmos. Sci*., vol.54, pp.1589–1598, 1997.

[28] E. K. M. Chang, GCM, and observational diagnoses of the seasonal and interannual variations of the Pacific storm track during the cold season, *J. Atmos. Sci*., vol.58, pp.1784–1800, 2001.

[29] M. A. Shapiro, and D. Keyser, Fronts, jet streams and the tropopause in *Extratropical Cyclones, The Erick Palmen Memorial Volume*, C. Newton and E. O. Holopainen, Eds., Amer. Meteor. Soc., pp.167–191, 1990.

[30] P. J. Neiman, M. A. Shapiro, and L. F. Fedor, The life cycle of an extratropical marine cyclone. Part II: mesoscale structure and diagnostics, *Mon. Wea. Rev*., vol.121, pp.2177–2199, 1993.

[31] P. J. Neiman, and M. A. Shapiro, The life cycle of an extratropical marine cyclone. Part I: Frontal-cyclone evolution and thermodynamic air-sea interaction, *Mon. Wea. Rev*., vol.121, pp.2153–2176, 1993.

[32] A. J. Simmons, Numerical simulations of cyclone life cycle in *The Life Cycles of Extratropical Cyclones*, M. A. Shapiro and S. Gronas, Eds., Amer. Meteor. Soc., pp.123–138, 1999.

[33] J. Bjerknes, and H. Solberg, Life cycle of cyclones and the polar front theory of atmospheric circulation, *Geofys. Publ*., vol.3, pp.1–18, 1922.

[34] T. N. Carlson, Airflow through midlatitude cyclones and the comma cloud pattern, *Mon. Wea. Rev*., vol.108, pp.1498–1509, 1980.

[35] K. A. Browning, Organization of clouds and precipitation in extratropical cyclones in *Extratropical Cyclones, The Erick Palmen Memorial Volume*, C. Newton and E. O. Holopainen, Eds., Amer. Meteor. Soc., pp.129–154, 1990.

[36] K. A. Browning, Mesoscale aspects of extratropical cyclones: An observational perspective in *The Life Cycles of Extratropical Cyclones*, M. A. Shapiro and S. Gronas, Eds., Amer. Meteor. Soc., pp.123–138.

[37] E. F. Danielsen, Stratosphere-troposphere exchange based upon radioactivity, ozone and potential vorticity, *J. Atmos. Sci*., vol.25, pp.502–518, 1968.

[38] M. V. Young, G. A. Monk, and K. A. Browning, Interpretation of satellite imagery of a rapidly deepening cyclone, Quart. *J. Roy. Meteor. Soc*., vol.113, pp.1089–1115, 1987.

[39] P. V. Hobbs, T. J. Matejka, P. H. Herzegh, J. D. Locatelli, and R. A. Houze, Jr., The mesoscale and microscale structure and organization of clouds and precipitation in midlatitude cyclones. I: A case study of a cold front, *J. Atmos. Sci*., vol.37, pp.568–596, 1980.

[40] C. D. Thorncroft, B. J. Hoskins, and M. E. McIntyre, Two-paradigms of baroclinic-wave life cycle behavior. *Quart. J. Roy. Meteor. Soc*., vol.119, pp.17–55, 1993.

[41] K. Ninomiya, Polar/comma-cloud lows over the Japan Sea and the Northwestern Pacific in winter, *J. Meteor. Soc. Japan*, vol.67, pp.307–317, 1989.

[42] K. Ninomiya, and K. Hoshino, Evolution process and multi-scale structure of a polar low developed over the Japan Sea on 11–12 December 1985. Part II: Meso-β-scale low in meso-α-scale polar low, *J. Meteor. Soc. Japan*, vol.68, pp.83–97, 1990.

[43] R. J. Reed, Cyclogenesis in polar air streams, *Mon. Wea. Rev*., vol.107, pp.38–52, 1979.

[44] S. Businger, The synoptic climatology of polar-low outbreaks, *Tellus*, vol.37A, pp.419–432, 1985.

[45] M. Nagata, On the structure of a convergent cloud band over the Japan Sea in winter, *J. Meteor. Soc. Japan*, vol.65, pp.871–883, 1987.

[46] K. Ninomiya, J. Fujimori, and T. Akiyama, Multi-scale features of the clod air outbreak over the Japan Sea and the Northwestern Pacific, *J. Meteor. Soc. Japan*, vol.74, pp.745–761, 1996.

[47] K. Ninomiya, and T. Akiyama, Muti-scale features of Baiu, the summer monsoon over Japan and the east Asia, *J. Meteor. Soc. Japan*, vol.70, pp.467–495, 1992.

[48] Y. Kawatani, and M. Takahashi, Simulation of the Baiu front in a high resolution AGCM, *J. Meteor. Soc. Japan*, vol.81, pp.113–126, 2002.

[49] K. Saito, Semi-implicit fully compressible version of the MRI mesoscale nonhydrostatic model – forecast experi-

ment of the 6 August 1993 Kagoshima torrential rain –, *Geophys. Mag*., vol.2, pp.109–137, 1997.

[50] T. Kato, and H. Goda, Formation and maintenance processes of a stationary band-shaped heavy rainfall observed in Niigata on 4 August 1998, *J. Meteor. Soc. Japan*, vol.79, pp.899–924, 2001.

[51] B. J. Hoskins, and F. P. Bretherton, Atmospheric frontogenesis models: mathematical formulation and solution, *J. Atmos. Sci*., vol.29, pp.11–37, 1972.

[52] K. Ninomiya, Characteristics of the Baiu front as a predominant subtropical front in summer Northern Hemisphere, *J. Meteor. Soc. Japan*, vol.62, pp.880–894, 1984.

[53] K. Ninomiya, and K. Yamazaki, Heavy rainfall associated with frontal depression in Asian subtropical humid region. Part II: mesoscale features of precipitation, radar echoes and stratification, *J. Meteor. Soc. Japan*, vol.57, pp.399–413, 1979.

[54] Y. Kurihara, R. T. Tuleya, and M. A. Bender, The GFDL Hurricane Prediction System and its Performance in the 1995 Hurricane Season, *Mon. Wea. Rev*., vol.126, pp.1306–1322, 1998.

[55] S. G. Gopalakrishnan, D. P. Bacon, N. N. Ahmad, Z. Boybeyi, T. J. Dunn, M. S. Hall, Y. Jin, P. C. S. Lee, D. E. Mays, R. V. Madala, A. Sarma, M. D. Turner, and T. R. Wait, An operational multiscale hurricane forecasting system, *Mon. Wea. Rev*., vol.130, pp.1830–1847, 2002.

[56] M. Nagata, L. Leslie, H. Kamahori, R. Nomura, H. Mino, Y. Kurihara, E. Rogers, R. L. Elsberry, B. K. Basu, A. Buzzi, J. Calvo, M. Desgagne, M. D'Isidoro, S.-Y. Hong, J. Katzfey, D. Majewski, P. Malguzzi, J. McGregor, A. Murata, J. Nachamkin, M. Roch, and C. Wilson, A mesoscale model intercomparison: A case of explosive development of a tropical cyclone (COMPARE III), *J. Meteor. Soc. Japan*, vol.79, pp.999–1033, 2002.

[57] B.G. Hunt, and S. Manabe, An investigation of thermal tidal oscillation in the earth-s atmosphere using a general circulation model, *Mon. Wea. Rev*., vol.96, pp.753–768, 1968.

[58] Y. Kurihara, and M. A. Bender, structure and Analysis of the Eye of a Numerically Simulated Tropical Cyclone, *J. Meteor. Soc. Japan*., vol.60, pp.381–395, 1982.

[59] F. Xiao, T. Yabe, X. Peng, and H. Kobayashi, Conservative and oscillation-less atmosphere transport schemes based on rational functions, *J. Geophys. Res*., vol.107 (D22), 4609, doi: 10.1029/2001JD001532.